Astronomy & Astrophysics manuscript no. output
August 3, 2020

Tidally perturbed pulsations in the pre-main sequence δ Scuti binary RS Cha

T. Steindl[1], K. Zwintz[1], D. M. Bowman[2]

[1]Institut für Astro- und Teilchenphysik, Universität Innsbruck, Technikerstraße 25, A-6020 Innsbruck, Austria
e-mail: thomas.steindl@uibk.ac.at
[2]Institute of Astronomy, KU Leuven, Celestijnenlaan 200D, B-3001 Leuven, Belgium

Received –; accepted –

ABSTRACT

Context. Stellar components in binaries are subject to tidal forces which influence the asteroseismic properties. Tidally pertubed pulsation have been reported for different objects but none of these are in their pre main sequence phase of evolution. This puts RS Cha, consisting of two δ Scuti stars, with pulsational characteristics influenced by tidal effects as the first such object observed.
Aims. We aim to investigate the pulsational properties of RS Cha in terms of the theory of tidally perturbed pulsations.
Methods. Based on photometric timeseries obtained from the TESS satellite, we perform binary modelling using `phoebe` to interpret the binary light curve and to allow the investigation of the pulsations of both components in RS Cha. We model the detrended light curve with two distinct theories: classical superposition of linear modes versus modes with phase dependent amplitudes, to disentangle the effect of tidally perturbed pulsation modes from the latter. The resulting lists of frequencies are then interpreted as self excited modes, affected by tidal perturbation.
Results. We find strong evidence for tidally perturbed modes that enable the identification of pulsation modes, both in the primary and the secondary component. Both components mainly pulsate in radial and dipole modes, while one prominent quadrupole mode is inferred for the secondary component. The latter verifies previous analysis from spectroscopic time series.
Conclusions. This work shows that RS Cha is an ideal binary to test the theory of tidally perturbed pulsation within the framework of asteroseismic modelling. The identification of multiple pulsation modes using this theory is unprecedented and will be a keystone in the future of pre-main sequence asteroseismology.

Key words. Asteroseismology.– Techniques: photometric.– Stars: individual: RS Cha – Stars: variables: delta Scuti – Stars: pre-main sequence – (Stars:) binaries: eclipsing.

1. Introduction

Asteroseismology – the study of stellar pulsations – is an important tool in studying stellar structure and evolution (Aerts et al. 2010). The capabilities of asteroseismic tools are inherently dependent on the type of pulsators and therefore the evolutionary stage of the star. Stars with convective envelopes (e.g. red giants) are subject to stochastic driving of modes which leads to solar-like oscillations that follow simple scaling relations allowing a robust determination of the star's size, weight and temperature (e.g. Chaplin & Miglio 2013; Aerts 2020; García & Ballot 2019). More sophisticated methods of analysis provide better estimates that are important for the classifications of exoplanets (Lundkvist et al. 2018; Adibekyan et al. 2018). For solar-like pulsators, the presence of acoustic glitches in freqency spacings allow the derivation of helium abundances even if stars do not display helium spectral lines (Verma et al. 2014, 2017, 2019; Verma & Silva Aguirre 2019; Aerts 2020).

Such detailed analysis is confined to stars on the main sequence or later evolutionary stages. High-quality observations are much less frequent among pre-main sequence stars owing to their fast evolution towards the main sequence and their sky position. The latter is typically in crowded star-forming regions along the ecliptic, a region of the sky which e.g. the main Kepler mission (Koch et al. 2010) pointed away from (Zwintz 2017). Moreover, pre-main sequence stars are often subject to periodic or aperiodic variability caused by various types of activity such as from disks or magnetic fields further complicating detailed analysis (Zwintz 2019). The pre-main sequence evolution is a vital building block of a star's life connecting star formation to later evolutionary stages, starting from the zero age main sequence. It therefore plays a major role concerning, for example, the transport of angular momentum (Zwintz 2019).

A significant amount of known pre-main sequence pulsators are δ Scuti type objects. They are located within the classical instability strip (Rodríguez & Breger 2001) with effective temperatures in the range $6300 \leq T_{\rm eff} \leq 9000$ K and luminosities in the range $0.6 \leq \log(L/L_{\odot}) \leq 2.0$ (Buzasi et al. 2005) corresponding to effective surface gravities in the range $3.5 \leq \log(g) \leq 4.5$ at stellar masses in the range of approximately $1.5 \leq M/M_{\odot} \leq 3.5$ for pre-main sequence objects (Zwintz et al. 2014). δ Scuti type stars typically oscillate in radial and non-radial pressure modes (p-modes) and low-order gravity modes (g-modes), exhibiting periods throughout the range of 18 min to 8 h (e.g Pamyatnykh 2000; Bowman & Kurtz 2018; Antoci et al. 2019). Zwintz et al. (2014) showed the presence of a relationship between the pulsation properties and the evolutionary status for pre-main sequence stars. The recent work by Bedding et al. (2020) indicates that a similar relationship also exists for more evolved δ Scuti stars.

Such intermediate mass stars often exist in binary systems, which leads to interactions having substantial effect on their

Table 1. Stellar parameters and orbital parameter for RS Cha.

	Primary	Secondary	Reference
$M/M_\odot$	1.89(1)	1.87(1)	A05
	1.823(12)	1.764(12)	W13
$R/R_\odot$	2.15(6)	2.36(6)	A05
$T_{\rm eff}$ (K)	7638(76)	7228(72)	R00
	7926(150)	7330(100)	F06
$\log(L/L_\odot)$	1.15(9)	1.13(9)	A05
$\log(g)$ (cm s^{-2})	4.05(6)	3.96(6)	A05
$v \sin i$ (km s^{-1})	64(6)	70(6)	A05
	68(2)	72(2)	W13
expected	66(3)	72(3)	
P (days)	1.66988(2)		W13
i (°)	83.4(3)		CN80
$e \sin w$	−0.013(4)		CN80
[Fe/H]	0.017(1)		A05
age (Myr)	6^{+2}_{-1}		LS04

Notes. For some parameters, multiple sources are given.
References: A05: Alecian et al. (2005), W13: Woollands et al. (2013), R00: Ribas et al. (2000), F06: Frémat et al. (2006) , CN80: Clausen & Nordstrom (1980), LS04: Luhman & Steeghs (2004)

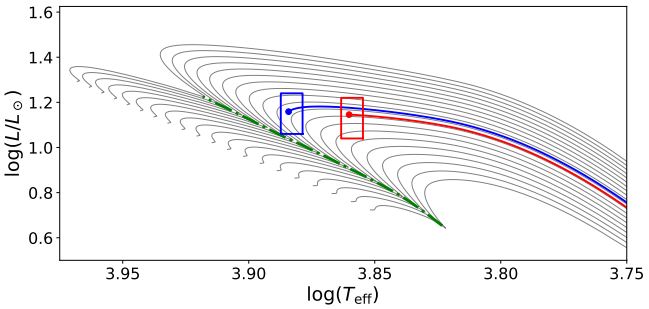

Fig. 1. The evolutionary status of the components of RS Cha in a Hertzsprung–Russell diagram. The grey lines show the evolutionary tracks of 1.6 $M_\odot$ to 2.0 $M_\odot$ stars towards the end of their pre-main sequence phase. The blue and red box shows the observational constraints for the primary and secondary respectively. Also shown are evolutionary tracks corresponding to masses reported by Alecian et al. (2005) that reproduce the observed radius at their final point (marked with a dot) for the primary (blue) and secondary (red). The green dash-dotted line marks the point of evolution where the central C^{12} mass fraction drops below 10^{-4}.

structure and evolution (see e.g. De Marco & Izzard 2017 for a review). These interactions moreover lead to deviations from sphericity and tidal effects, which in turn influence the seismic properties of the stars. For close binaries in an eccentric orbit, tidal effects can lead to the excitation of g-modes at multiples of the orbit frequency (Fuller 2017). This is typically observed in heartbeat stars (e.g. Welsh et al. 2011) or eclipsing binaries (e.g. Hambleton et al. 2013; Maceroni et al. 2014). Recently, Handler et al. (2020) and Kurtz et al. (2020) presented the cases of HD 74423 and CO Cam, where tidal forces modified the orientation of the pulsation axis leading to tidal trapping of the oscillations.

Tidal effects further lead to a deformation of the pulsation cavity that results in a perturbation of self-excited pulsation modes (Polfliet & Smeyers 1990; Reyniers & Smeyers 2003a,b). In the observers' frame, this leads to multiplets spaced by (twice) the orbital frequency (Smeyers 2005). Such perturbed modes have been observed in a handful of stars (Lee et al. 2016; Balona 2018; Bowman et al. 2019; Southworth et al. 2020; Jerzykiewicz et al. 2020) and probably also in the eclipsing binary discussed by Hambleton et al. (2013) as pointed out by Balona (2018).

In this work, we present an asteroseismic analysis of the pre-main sequence eclipsing binary system RS Cha, the first pre-main sequence objects showing evidence of tidal effects on the pulsation characteristics. This has been made possible by the stunning precision of light curves obtained by the *Transiting Exoplanet Transit Survey* (TESS; Ricker et al. 2015). In Section 2 we discuss the system RS Cha and the previous publications focusing on the orbital and stellar parameters as well as the pulsation characteristics. Section 3 describes the observations that were used in the analysis. Section 4 describe the binary light curve modelling. We explain the frequency analysis and discuss tidal effects on the light curve of RS Cha in Section 5.

2. The Eclipsing Binary System RS Cha

2.1. Orbital and Stellar Parameters

Cousins (1960) first reported RS Cha to be a variable star with visual magnitude in the range of 6.02 to 6.05 at a spectral type A5. Only four years later, Strohmeier (1964) was the first to discover the binary nature of RS Cha, denoting it as eclipsing binary of either Algol or β Lyrae type. Later efforts of multiple contributors led to the determination of the orbit and stellar parameters for both stars, summarized by Alecian et al. (2005). The latter furthermore presented a detailed analysis in terms of stellar calibration of the two individual components in a series of publications (Alecian et al. 2006, 2007a,b). They conclude that RS Cha is composed of two pre-main sequence stars in an evolutionary phase at the first onset of CNO-burning. At this evolutionary stage, central conditions lead to a C^{12} depletion by the first steps of the CNO cycle ($C^{12}(p,\gamma)N^{13}(\beta^+,\nu)C^{13}(p,\gamma)N^{14}$). The formation of a convective core produces the well known hook in the evolutionary track before the stars arrival at the zero-age main sequence (Iben 1965). Furthermore, they report the need to reduce the abundance of nitrogen and carbon with respect to the Sun to match the observations.

RS Cha is a circularized and synchronized (Alecian et al. 2005; Woollands et al. 2013) binary system of two components of similar mass and luminosity. The orbital and stellar parameters are given in Table 1 and the synchronization result is implied by a $v \sin i$ ratio equal to the ratio of the radii, the circular orbit (Clausen & Nordstrom 1980) and the expected timescales (Zahn 1977; Mayer & Hanna 1991). Woollands et al. (2013) reported a high probability, that is with a 99.9 percent confidence, that a third component exists within the system, with a mass ranging from 0.3 to 0.52 $M_\odot$ and absolute magnitude ranging from M_v = 24.96 to 30.32. This would correspond to the third body being either a white or red dwarf, with the latter being most likely given the evolutionary timescales.

Figure 1 shows the evolutionary status of RS Cha using the result of Alecian et al. (2007a). The colored lines show stellar evolution tracks that match the observational constraints at a common age of 9.15 Myr. This is close to the 9.5 Myr reported by Alecian et al. (2007a). Luhman & Steeghs (2004) report an age of 6^{+2}_{-1} Myr that stems for isochrone fitting and is just below this value. The evolution models in Figgure 1 were calculated with version 12778 of *Modules for Experiments in Stellar Astrophysics* (`MESA`; Paxton et al. 2011, 2013, 2015, 2018, 2019).

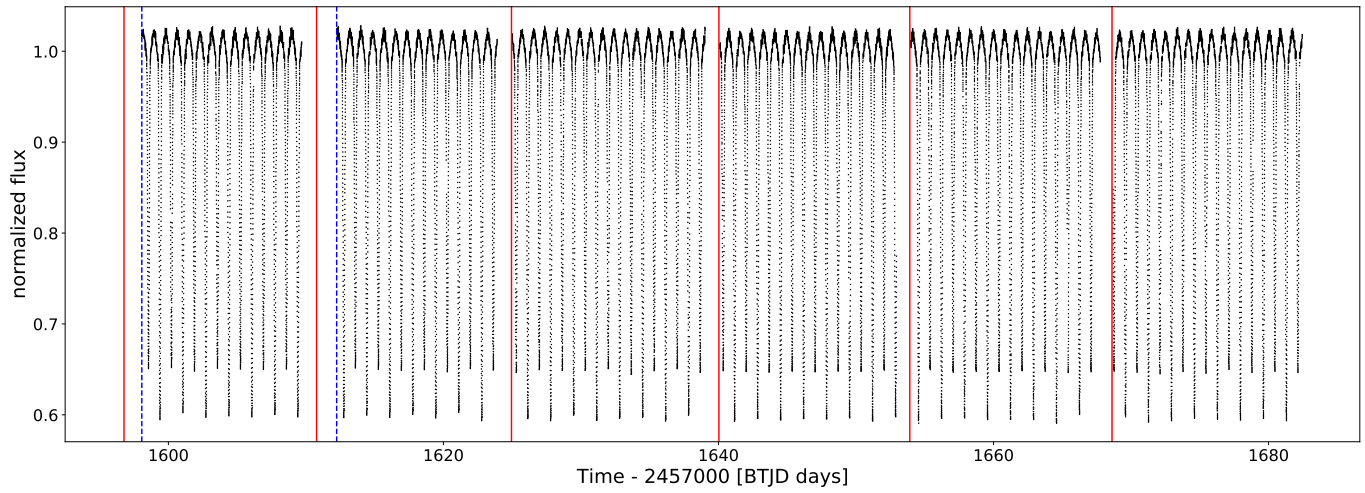

Fig. 2. The SAP FLUX light curve of RS Cha as black dots. Vertical red lines mark the start of any Orbits. Orbits 29 and 30 in sector 11 suffered from scattered light signals. The corresponding measurements have been removed by the TESS pipeline. This concerns the times between the start of the orbits and the blue dashed lines.

2.2. Pulsations

Initially observed as part of a program to detect new δ Scuti stars, McInally & Austin (1977) were the first to report short-period variability in the light curve of RS Cha. They concluded that at least one component is a δ Scuti star. Clausen & Nordstrom (1980) obtained a 22-d light curve consisting of 1001 individual observations. They found that both components are δ Scuti stars although they were not able to report a definitive decision. Furthermore, they reported the three most obvious periods: 0.094 d, 0.086 d, and 0.072 d corresponding to frequencies: 10.64 d^{-1}, 11.63 d^{-1}, and 13.89 d^{-1}.

Alecian et al. (2005) investigated radial velocity curves and found regular variations in both components. Because their observations spanned less than 3 h per night, they were not able to reliably find any pulsation period (Alecian et al. 2005). Still, they report 22.079 d^{-1}as the most prominent variation for the primary component.

Böhm et al. (2009) observed RS Cha for 14 nights with the high-resolution echelle spectrograph Hercules at the Mt John telescope in New Zealand. They reported the first clear detection of pulsation frequencies, both for the primary and secondary component. According to their spectroscopic analysis, the primary component shows high degree ($l = 8-11$) pulsation modes with frequencies 21.11 $d^{-1}$and 30.38 d^{-1}while the secondary component shows pulsation modes with 12.81 d^{-1}(l = 2 or 3), 19.11 d^{-1}(l = 0, 10 or 13), and 24.56 d^{-1}(l = 6).

3. Observations - TESS Data

The *Transiting Exoplanet Transit Survey* (TESS; Ricker et al. 2015) is an MIT-led NASA mission designed for the discovery of planetary transits. The all-sky survey delivers high-quality light curves for more than 200000 stars, rendering it very useful for asteroseismology. RS Cha (TIC 323292655) has been observed by TESS as part of the TASC_WG04_SC proposal aiming at studying δ Scuti stars. The photometric observations of RS Cha embody four sectors, each observed for two spacecraft orbits (27.4 d) (Ricker et al. 2015). The resulting data product consists of one sector of full frame images (sector 10) and three sectors of short cadence data (sectors 11, 12, 13). For our analysis, we used the short cadence data spanning a total of 84.28 d. These data are taken with an exposure time of 2 s and then stacked at a cadence of 2 min.

We accessed the light curve of RS Cha from the Michulski Archive for Space Telescopes with the python package `lightkurve` (Barentsen et al. 2019). We used the simple aperture photometry (SAP flux; Morris et al. 2017), combined the sectors and normalized the data set according to the median. The SAP flux was preferred over the PDCSAP flux because the co-trending basis vector analysis introduces instrumental effects especially in sector 12. The resulting light curve is shown in Figure 2, where the eclipsing nature of the binary is clearly visible. The light curve consists of a total of 55309 points with 5 gaps. These gaps are due to data downlink in between orbits (see red lines in Figure 2) as well as omitted points because of scattered light from the earth (see blue dashed lines in Figure 2). The gaps have a duration of 2.55, 1.06, 1.04, 1.02 and 0.93 day, resulting in a duty cycle of 92.1 %. Furthermore, TESS pixels are comparably large and we might expect contamination from nearby sources. The contamination is given as 0.03, therefore we expect that the data does not suffer from strong third light effects. Figure 3 shows a zoom in first part of sector 12, emphasizing the out-of-eclipse light curve. Pulsational variability of the light curve is clearly visible. The strongest modulation is of the order of 2 to 3 h, therefore clearly indicating pressure modes and δ Scuti type pulsations.

4. Binary Modelling

We use the next generation Wilson-Devinney code *Physics Of Eclipsing Binaries* (`PHOEBE`; Prša & Zwitter 2005; Prša et al. 2016; Horvat et al. 2018; Jones et al. 2019) version 2.2.1 to calculate theoretical light curve models for the eclipsing binary. Because the orbital parameters are well constrained (see Table 1), the aim of the binary modelling is to remove the eclipsing binary signal from the light curve to extract only the pulsational signal.

To do so, we implemented a Nelder-Mead algorithm (Nelder & Mead 1965), a direct search algorithm often used for optimization problems with unknown derivatives. The algorithm is further described in Appendix A. We used an 8−dimensional parameter space including the mass, equivalent radius, and effec-

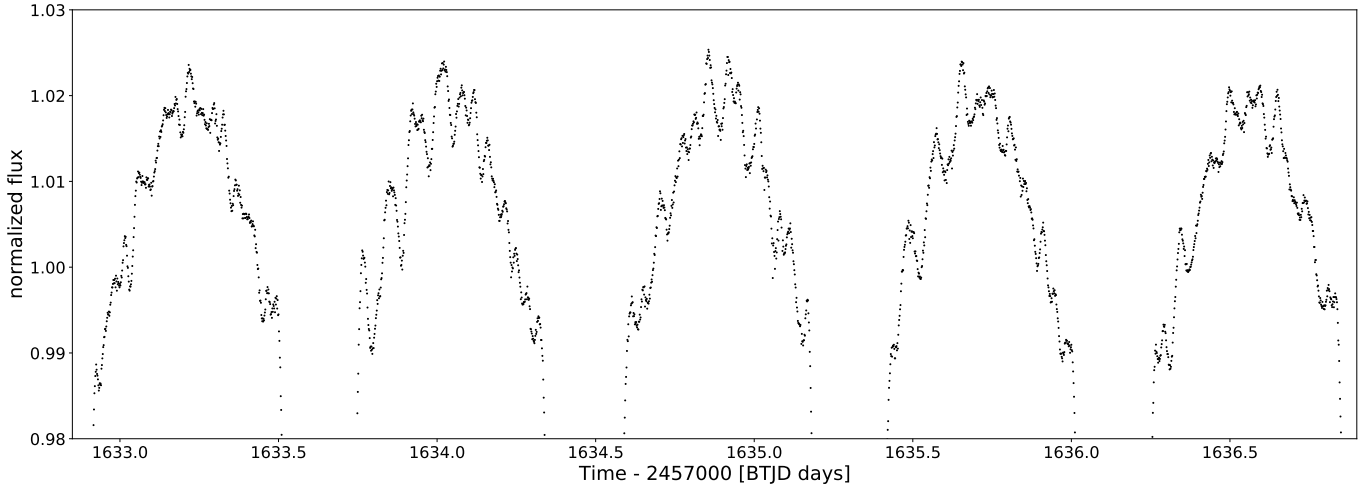

Fig. 3. A zoom in the light curve to make the out-of-eclipse phase variations more visible. The pulsation variations (hours) can clearly be seen.

tive temperature for both the primary and the secondary component as well as the inclination of the system and the time of superior conjunction to optimize a first binary model. The initial values for the mass, equivalent radius, effective temperature, and inclination were taken from Table 1 (references A05 and R00) and we fitted the first primary eclipse with a Gaussian function to obtain an initial value for the time of superior conjunction. The other parameters, which might be different from PHOEBEs default binary, are kept constant during the iterations and can be found in Table 2. The value for the period was found by applying a phase dispersion minimization algorithm (Stellingwerf 1978) on the light curve. We find that aggressive coefficients (see A) work best in obtaining good models for the eclipsing light curve after 1000 iterations. We use a third of the light curve, that is sector 11 and the start of sector 12 to find a good consensus between using most of the available data and execution time.

The residuals show more than 100 frequencies that are significant in a classical Fourier analysis, some of which were multiples of the orbital frequency. Because both components are δ Scuti type stars, a comparable number of frequencies may be expected. The remaining variance at integer multiples of the orbital frequency may be attributed to an inadequate orbital solution because the quality of TESS observations are so good, that the uncertainties are dominated by the choices in the binary modelling. We pre-whitened the light curve for the frequencies that are not multiples of the orbital frequency and applied a Savitzky-Golay filter (Savitzky & Golay 1964) with a window length of 12001 points to remove irregular low frequency variations before any further optimization.[1] Such a process is typical when modelling binary stars with pulsating components (see e.g. Hambleton et al. 2013). The process consists of multiple iterations until the light curve is thoroughly pre-whitened from any pulsation signal. In this particular case, one iteration of pre-whitening is sufficient.

We used the new binary light curve (the light curve minus the frequencies and the Savitzky-Golay filter) to determine the most precise values for the period and time of superior conjunction by creating an O−C diagram. The calculated values for the primary (and secondary) eclipse were obtained as $t_0 + iP$ ($t_0 + (i + \frac{1}{2}P)$ where t_0 is the time of superior conjunction and P is the period. We optimized both t_0 and P to find the most precise parameters. The resulting O−C diagram is shown in Figure 4. The best fitting values are a period of 1.66987725(5) d and a time of superior conjunction of 1599.397275(5) + 2457000 BTJD. Thus, these values were fixed in the final optimization.

We included gravity darkening and Lambert scattering (irradiation method Horvat (Prša et al. 2016)) in the final Nelder-Mead optimization. Including the gravity darkening coefficients and the ratio of bolometric light reflected/irradiated by the stars adds four dimensions to the parameter space. All of these values were set to 0.5. On the other hand, we dropped the time of superior conjunction in the optimization, leading to a 11-dimensional parameter space.

Figure 5 shows a phase folded and binned version of the full light curve together with the result of the Nelder-Mead optimization. The residuals show that even with the inclusion of gravity darkening and Lambert scattering the light curve cannot be reproduced perfectly. Therefore, we fitted the remaining residuals with frequencies up to the first 30 orbital harmonics. The subtraction of this fit yields the residuals in the lower panel of 5. To obtain the final light curve for the pulsation analysis we calculated a binary model and subtracted it from the full light curve. In addition, the fitted orbital harmonics and a Savitzky-Golay filter were subtracted. The result of this analysis is hereafter called pulsation light curve.

5. Pulsation Analysis

The lightcurve resulting from binary modelling demonstrates clear pulsations in the region 10 $d^{-1}$to 30 d^{-1}as can be seen from the amplitude spectrum (see middle panel of Figure 6). We used `smurfs` (Müllner 2020) and our own codes to generate amplitude spectra and to perform the pulsation analysis. The TESS magnitude of RS Cha is 5.6. The expected point to point scatter for sectors 11, 12 and 13 is 165 parts per million (ppm) for short-cadence data at this magnitude. We therefore attribute an average error of this value to the observed flux. In the following, we will differentiate between frequencies with high amplitudes (> 165 ppm) and frequencies with low amplitudes (≤ 165 ppm).

A traditional Fourier analysis reveals more than 100 significant frequencies in the range of 0.1 $d^{-1}$to 34 d^{-1}, with amplitudes varying between 1671 and 80 ppm. Upon closer inspection, we find strong amplitude variation throughout the duration

[1] With this window length, the procedure removes intrinsic variability $\lesssim 0.15$ $d^{-1}$and does not influence subsequent analysis concerning pulsations.

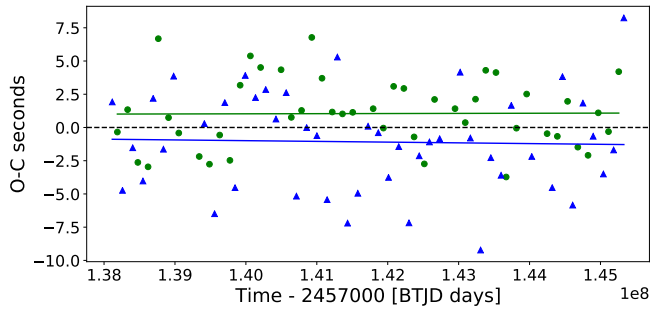

Fig. 4. The eclipse timing variations for the light curve after the first iteration. The green circles and blue triangles show the values for the primary and secondary eclipse respectively. Both data were fitted with a straight line. The small offset to the expected values (black dashed line) could indicate a slight non-zero eccentricity.

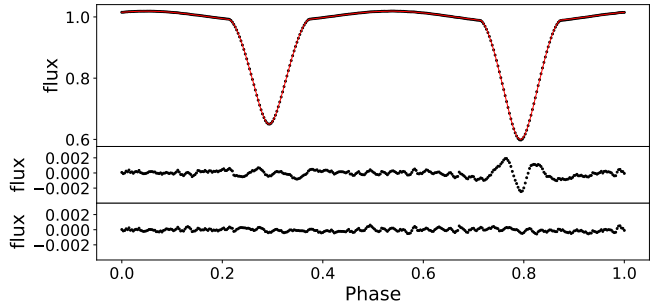

Fig. 5. Top panel: The binned and phase folded observed light curve (black dots) and the final PHOEBE model (red line). Middle panel: The residuals of the best fitting model. Lower panel: The residuals after also removing the fitted orbital harmonics

of the observations, which is reasonable given the changing geometry of a pulsating eclipsing binary system. We further investigated this amplitude variation to include its effect in the interpretation of the pulsation analysis. We find that the amplitude is strongly dependent on the binary phase and discuss this in Section 5.1. Such effects have strong implications on the frequencies extracted from classical Fourier analysis and specifically lead to alias peaks with signature comparable to tidal effects. Similar to the work of Degroote et al. (2009) who analysed the light curve of a large amplitude β Cep star with different models, we analyse the light curve of RS Cha with two distinct models. First, we perform a traditional Fourier analysis in Section 5.2. Second, we analyse the light curve in terms of a model in which the amplitudes are dependent on the orbital period (hereafter phase dependent amplitudes) in Section 5.3 before we use statistical criteria to compare the results in section 5.4. The information obtained by this analysis has crucial implications on the interpretation in Section 6.

5.1. Binary Phase Dependent Amplitudes

Figure 6 compares the amplitude spectra of different versions of the light curve on the left and the corresponding phase folded light curve on the right of each panel. The top panel shows the amplitude spectra of the original light curve, which is dominated by the eclipsing binary signal. The highest peaks are found at two, four, six, eight and ten times the orbital frequency with amplitudes strongly decreasing towards higher multiples. Furthermore, some small amplitude signal in the range of 10 to 15 $d^{-1}$and around 20 $d^{-1}$is visible. In comparison, the middle panel shows the pulsation light curve which demonstrates clear pulsations especially between 10 $d^{-1}$and 15 $d^{-1}$and between 18 $d^{-1}$and 28 d^{-1}. The corresponding phase folded light curve shown on the right of the middle panel indicates significant amplitude variations due to the eclipsing nature of RS Cha. During secondary eclipse (and to a smaller extent also during primary eclipse), the pulsation amplitude is clearly diminished. This change in amplitude during eclipses can also be seen in the amplitude spectrum of the out-of-eclipse light curve which is shown in the bottom panel.

To further investigate this change in amplitude, we fitted the five highest peaks (11.07, 11.62 d^{-1}, 12.79 d^{-1}, 20.122 d^{-1}, 18.92 d^{-1}) to subsets of the pulsation light curve. The subsets are defined by the orbital phase of the timestamps. We used timestamps with $\phi \pm \Delta\phi$ where ϕ is the orbital phase and $\Delta\phi = 0.05$. This subsets include about 5500 data points each. The results for the three frequencies with the highest amplitude are shown in Figure 7. The amplitudes of F1 and F3 (top and third panels) show a similar variation: a roughly constant value in phases between 0.4 and 0.2 and a sharp decrease during secondary eclipse. This indicates that both frequencies originate from the secondary component. Indeed, the frequency of F3, 12.8 $d^{-1}$is very close to the $l = 2$ or 3 mode reported by Böhm et al. (2009), which we would expect to see in photometry. The uncertainties on the amplitudes is a combination of the uncertainties reported by the least squares fitting algorithm and the standard error estimate $\sigma_A = \sqrt{\frac{2}{N}}\sigma_n$ where N is the number of points in the subset light curve and σ_n the root mean square deviation of the observed flux(Montgomery & O'Donoghue 1999). Since this standard error estimate is for data without aliasing problem and the spectral window of this subset light curves is sub-optimal with a duty cycle below 10% we expect this values to be underestimated. Correlation of the measured data points lead to additional underestimation of the uncertainty(Degroote et al. 2009).

Table 2. Fixed parameters that might be different from PHOEBEs default binary used in our Nelder-Mead optimization.

Parameter	Value
orbital period (days)	1.66987725
t_0 (+2457000 BTJD days)	1599.397275
eccentricity (°)	0
Synchronicity parameter Primary	1
Synchronicity parameter Secondary	1
pblum_mode	dataset-scaled
passband	TESS:T
irrad_method	horvat

Notes. t_0 refers to the time of superior conjunction. Short descriptions of some parameters[a]: The pblum_mode defines how the passband intensities are handled, where dataset_scaled refers to a method that scales the resulting model to best fit the data. The option passband defines which passband is used for the calculations of luminosities, where we use the passband developed for data obtained by TESS. The passband was downloaded from the available online passbands. The option irrad_method defines which method to use for the handling of irradiation, where we used the Horvat scheme.

[a] See `http://phoebe-project.org/docs/2.2/physics` for more details

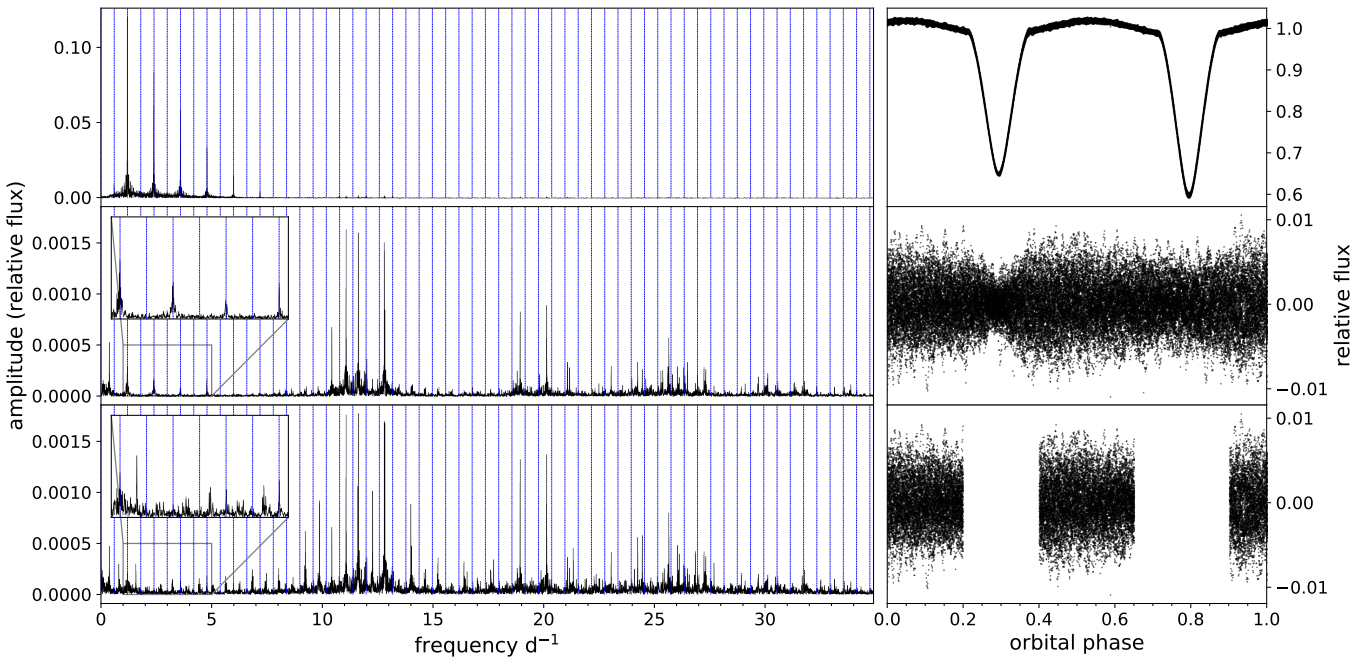

Fig. 6. Amplitude spectra and phase folds for different light curves. Top panel: The original light curve. Middle panel: The light curve minus the binary model. Bottom panel: The light curve minus the binary model in the out-of-eclipse phase. The middle and bottom panel have the same scaling in the y-axis while the scaling of the top panel is different.

Due to the shape of the decrease, we tried to fit the values in Figure 7 with a negative Gaussian peak with constant offset. Using only the area of the secondary eclipse, the fit agrees well with the data for F1 and F3, but not at all for F2 (as can be seen from the reduced chi-square statistic $\frac{\chi^2}{\mathrm{red}}$). We simulated light curves with such phase dependent amplitudes and similar frequencies and found that the result for F2 is strongly affected by the presence of other frequencies in the amplitude spectrum. The fourth panel in Figure 7 shows a convolution of F1 and F3 where the amplitude is shown in units of the mean throughout the phases. Here, we fitted the Gaussian peak to all data points. Again, the decrease at secondary eclipse fits very well, although the out-of-eclipse phase does not fit in a comparative manner. This results in a reduced chi-square of $\frac{\chi^2}{\mathrm{red}} = 4.87$ which would indicate that the model does not fit data well.

We further investigated the possibility of such amplitude modulation by calculating amplitude spectra of simulated light curves and comparing them to the amplitude spectra of the pulsation light curve. The phase dependent amplitude leads to side peaks in the amplitude spectrum at $\pm i f_{\mathrm{orb}}$ where i is an integer and f_{orb} the orbital frequency. Such a modulation is also evident in the amplitude spectrum of the pulsation light curve.

Therefore, we model the light curve of RS Cha both with a superposition of linear modes as well as with a superposition of modes with phase dependent amplitudes. Similar to the work of Degroote et al. (2009) we use the variance reduction (VR), power reduction (PR), Akaike's information criterion (AIC) and the Bayesian information criterion (BIC) to compare the different models and their goodness of fit respectively. A description of these criteria can be found in Section 3.4 of Degroote et al. (2009).

5.2. Superposition of linear modes

The first model considered is the classical superposition of linear modes. This resembles the traditional Fourier analysis. The model flux is given by

$$M_1(t_j) = c + \sum_{i=1}^{n} A_i \sin\left[2\pi(f_i t_j + \phi_i)\right] \quad (1)$$

for n frequencies, where A_i, f_i and ϕ_i denote the amplitude, frequency and phase of the i-th frequency respectively. Furthermore, c is constant offset that is set to zero for our analysis. The model is evaluated at every observation time t_j. Thus, this model has a total of $3n$ free parameters.

The model is produced in an iterative process. In every iteration, a Lomb-Scargle periodogramm (Lomb 1976; Scargle 1982) is calculated and the frequency and the amplitude of the highest peak is detected. These, and an initial phase of 0.5, are used to fit a single sine to the residual and the corresponding sine is subtracted from the latter. If the amplitude exceeds four times the local noise level, the frequency is considered to be significant and added to the list of model frequencies (Breger et al. 1993; Kuschnig et al. 1997). At every iteration stage, all frequencies, amplitude and phases of the frequencies in the model are fitted to the pulsation light curve. The iterations were stopped when five consecutive frequencies were insignificant (i.e. S/N < 4).

The resulting model has a total of 108 significant frequencies, 45 of which show amplitudes higher than 165 ppm and are specified in Table 3. In this set of frequencies, we find two types of combinations: (i), combination with the orbital frequency and (ii), combinations with other frequencies. For every frequency F_i identified by the algorithm we therefore looked for possible combinations of frequencies with higher amplitudes in the form $\mathrm{F}_i = a\mathrm{F}_j + b\mathrm{F}_k$, where $a \in [-2, -1, 1, -2]$ and $b \in [-2, -1, 0, 1, -2]$. A combination was accepted as such , if the difference was below half of the Rayleigh limit $\frac{1}{T}$, where

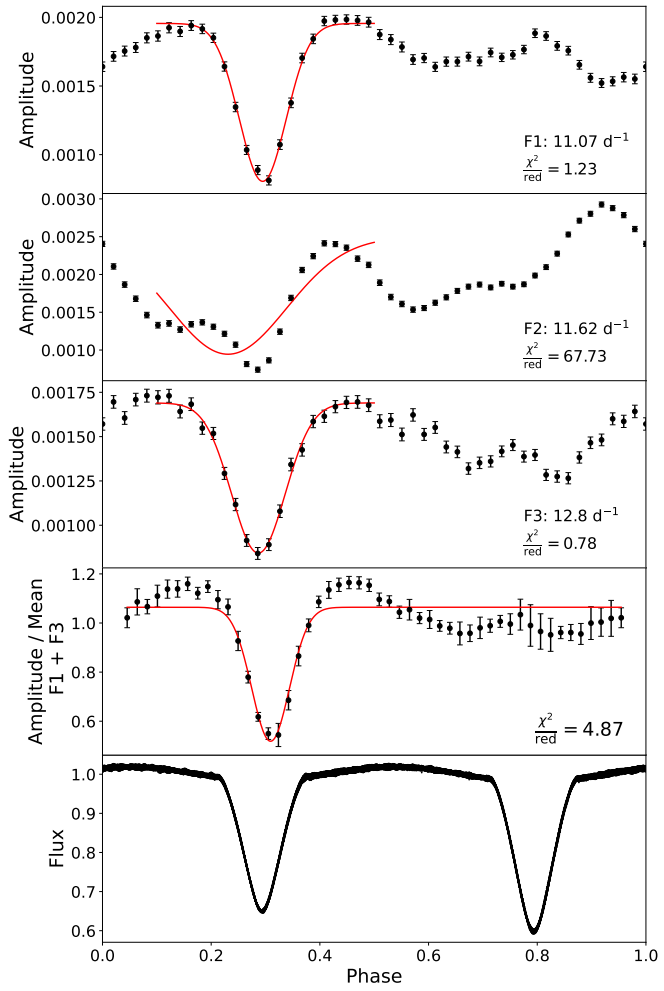

Fig. 7. The top three panels show the amplitude of the 3 frequencies with the highest amplitude in the Lomb-Scargle periodogram as a function of the orbital phase. Values in the phases between 0.1 and 0.5 are fitted with a negative Gaussian peak. The frequency and resulting reduced chi-square statistic is given in the bottom right of each panel. See the text for additional explanation how the frequencies were fitted. Fourth Panel: The amplitude divided by the mean combined for F1 and F3. The resulting values have been fitted and the reduced chi-square statistic is shown on the right bottom of the panel. Bottom panel: The phase folded light curve for comparison.

T is the total length of the light curve (Degroote et al. 2009). The identified combinations are shown in Table 3. We find 18 frequencies that are fully independent, mostly in the range of $10-13$ and $18-27$ d^{-1}. The full list of all frequencies extracted, independent of an amplitude cutoff, is shown in Table B.1.

Table 3 shows some low frequencies in the range of $0-5$ d^{-1}(F9, F10, F42, F44 and F45). The latter four are close to multiples of the orbital frequency of 0.59884 d^{-1}. While F42, F44 and F45 are found to be combination frequencies, F10 is independent according to the explanations above. F10 might have been introduced in the binary modelling (see Section 4). F9 is unrelated to the orbital frequency and corresponds to a period of 2.598 days. If the binary system would not be synchronized, this might be a signal of rotational variability of either component. A period of 2.598 days would correspond to a v sin i of 42(2) km s^{-1} and 46(2) km s^{-1} for the primary and secondary respectively. This does not fit the observed radial velocity measurements (see Table 1). We therefore exclude F9 to be a signal of rotational variability.

Table 3. The identified frequencies using superposition of linear modes and their corresponding amplitudes and phases.

Designation	f (d^{-1})	A (ppm)	ϕ ($\frac{\mathrm{rad}}{2\pi}$)	$f - if_{\mathrm{orb}}$ (d^{-1})
F1	11.070396(6)	1671(14)	0.881(6)	0.291161(6)
F2	11.624913(6)	1644(14)	0.951(7)	0.246831(6)
F3	12.795260(7)	1450(14)	0.898(10)	0.219486(7)
F4	20.122555(10)	909(14)	0.671(12)	0.238223(10)
F5=F4$-2f_{\mathrm{orb}}$	18.924924(11)	852(14)	0.654(12)	0.238161(11)
F6=F2$+2f_{\mathrm{orb}}$	12.822585(13)	751(14)	0.955(16)	0.246810(13)
F7=F2$-2f_{\mathrm{orb}}$	10.427359(13)	689(14)	0.416(16)	0.246970(13)
F8	25.636172(16)	586(14)	0.923(18)	0.114224(16)
F9	0.384953(17)	526(14)	0.911(20)	0.213894(17)
F10	1.20499(9)	355(6)	0.93(15)	0.00730(9)
F11=F2+F9	12.004905(29)	353(14)	0.14(4)	0.027977(29)
F12	21.064357(27)	336(14)	0.96(3)	0.104732(27)
F13	24.231017(27)	333(14)	0.84(3)	0.277161(27)
F14=F2$-f_{\mathrm{orb}}$	11.025846(28)	331(14)	0.17(3)	0.246610(28)
F15	26.474933(29)	320(14)	0.46(3)	0.125691(29)
F16=2F3	25.58853(3)	307(14)	0.43(4)	0.16187(3)
F17	26.02396(3)	304(14)	0.26(4)	0.27357(3)
F18=F13$-2f_{\mathrm{orb}}$	23.03406(3)	302(14)	0.70(4)	0.27790(3)
F19	21.15642(3)	296(14)	0.86(4)	0.19680(3)
F20	18.79018(3)	283(14)	0.45(4)	0.22594(3)
F21	26.30992(3)	278(14)	0.58(4)	0.03932(3)
F22	25.36344(3)	276(14)	0.93(4)	0.21189(3)
F23=F17$+2f_{\mathrm{orb}}$	27.22191(4)	267(14)	0.76(4)	0.27382(4)
F24=2F13$-$F19	27.30487(4)	265(14)	0.75(4)	0.24206(4)
F25=F15$-2f_{\mathrm{orb}}$	25.27759(4)	261(14)	0.48(4)	0.12604(4)
F26=F8$-2f_{\mathrm{orb}}$	24.43814(4)	259(14)	0.56(4)	0.11456(4)
F27=2F20$-$F8	11.94680(4)	255(14)	0.99(4)	0.03013(4)
F28	19.80501(4)	235(14)	0.59(4)	0.04308(4)
F29=2F10	2.40437(15)	228(10)	0.53(25)	0.00899(15)
F30=F1$+3f_{\mathrm{orb}}$	12.86744(4)	226(14)	0.68(5)	0.29167(4)
F31=F10+2F30	26.93439(4)	213(14)	0.69(5)	0.01370(4)
F32	30.10391(5)	203(14)	0.89(6)	0.16159(5)
F33=F26$-$F27	12.49486(5)	195(14)	0.84(5)	0.08091(5)
F34=F33$-f_{\mathrm{orb}}$	11.89432(5)	193(14)	0.79(6)	0.08261(5)
F35=F24$-2f_{\mathrm{orb}}$	26.10775(5)	190(14)	0.90(6)	0.24149(5)
F36	25.79572(5)	188(14)	0.45(6)	0.04533(5)
F37=F3$-$2F9	12.01945(6)	184(14)	0.41(7)	0.04252(6)
F38	29.67863(6)	184(14)	0.11(8)	0.26369(6)
F39=2F8$-$F24	23.96734(5)	182(14)	0.62(6)	0.01348(5)
F40=2F3+2F9	26.36555(5)	182(14)	0.31(6)	0.01631(5)
F41=F36$-2f_{\mathrm{orb}}$	24.59721(5)	180(14)	0.41(6)	0.04451(5)
F42=F26$-$2F2	1.19073(9)	179(18)	0.75(14)	0.00696(9)
F43=2F29+F25	30.09140(6)	178(14)	0.69(7)	0.14908(6)
F44=2F6$-$F26	1.21202(16)	175(6)	0.81(25)	0.01433(16)
F45=F8$-$2F7	4.78401(5)	167(14)	0.45(6)	0.00676(5)

Notes. The values in parentheses give the 1σ uncertainty as a combination of the values reported by the least square algorithm and the standard error estimates formulated by Montgomery & O'Donoghue (1999). f_{orb} is the orbital frequency. Further possible combinations are: F24=2F15$-$2F6; F33= F22$-$F30; F37=2F12$-$F32; F39=F27+F37; F43=2F26$-$F20; F44=F29$-$F42; F45=F29+2F42

Table 4. The parameters for the phase dependent amplitudes of model M_2.

Component	ϕ_0 ($\frac{\text{rad}}{2\pi}$)	σ ($\frac{\text{rad}}{2\pi}$)	δ	#
Primary	0.7913(4)	0.0481(4)	0.511(3)	14
Secondary	0.29098(8)	0.02768(9)	0.6470(16)	32

Notes. The values in parentheses give the 1σ uncertainty as reported by the least square algorithm. # denotes the number of frequencies with amplitudes higher than 165 ppm identified for each component.

5.3. Superposition of modes with phase dependent Amplitude

In this alternative model (M_2), the amplitude is dependent on the orbital phase. The decrease in amplitude is described by a negative Gaussian peak at the time of eclipse. Therefore, any frequency is assigned to either the primary or secondary star. The model flux is given by

$$M_2(t_j) = c + \sum_{i=1}^{n_\mathrm{p}} A_i\, D(t_j, \delta_\mathrm{p}, \phi_{0,\mathrm{p}}, \sigma_\mathrm{p}) \sin\left[2\pi(f_i t_j + \phi_i)\right] + \\ + \sum_{k=1}^{n_\mathrm{s}} A_k\, D(t_j, \delta_\mathrm{s}, \phi_{0,\mathrm{s}}, \sigma_\mathrm{s}) \sin\left[2\pi(f_k t_j + \phi_k)\right], \quad (2)$$

where

$$D(t, \delta, \phi_0, \sigma) = 1 - \delta \exp\left[-\left(\frac{t \text{ modulo } P}{P} - \phi_0\right)^2 / (2\sigma^2)\right], \quad (3)$$

describes the decrease in amplitude during eclipses. Here, n_p (n_s) is the number of frequencies assigned to the primary (secondary) component, the meaning of c is as in equation (1), δ describes the amount of the amplitude decrease, ϕ_0 the orbital phase of the minimum, σ the standard deviation of the Gaussian and P = 1.66987725 d the orbital period of the system. As in equation (1), A_i, f_i and ϕ_i denote the amplitude, frequency and phase of the i-th frequency respectively. The subscripts p and s correspond to values for the primary and secondary.

The model has a total number of $3n_\mathrm{p} + 3n_\mathrm{s} + (3)_\mathrm{p} + (3)_\mathrm{s}$ free parameters, where the parentheses denote that this numbers are only added if there is at least one frequency assigned to the primary or secondary component respectively. Appendix C further discusses light curves generated with this model and its amplitude spectra.

Similar to the superposition of linear modes, the model is produced in an iterative process. An initial guess is extracted from the amplitude spectrum of the residuum and fitted to the residual light curve with the function for phase dependent amplitude

$$\mathrm{PDA}(t_j) = A\, D(t_j, \delta, \phi_{0,\mathrm{p/s}}, \sigma) \sin\left[2\pi(f t_j + \phi)\right]. \quad (4)$$

The initial values and constraints for δ and σ are 0.75 ± 0.15 and 0.05 ± 0.025 and the fit is produced for a primary and a secondary model taking the values and constraints $\phi_{0,\mathrm{p}} = 0.8 \pm 0.05$ and $\phi_{0,\mathrm{s}} = 0.3 \pm 0.05$ respectively. We then calculate the AIC, BIC, VR and PR for both of the fits and use this statistics to assign the frequency to a star. In the assignment, the AIC and the BIC are the preferred statistics. The frequency is again only added to the model if the amplitude exceeds four times the local noise level (Breger et al. 1993; Kuschnig et al. 1997). The iterations were stopped when five consecutive frequencies were insignificant (i.e. S/N < 4). At every iteration stage all frequencies, amplitudes and phases for the frequencies in the model as well as the parameters for the phase dependent amplitude for the primary and secondary are fitted to the pulsation light curve with an iterative approach. First the modes of both stars are fitted to the pulsation light curve separately. Then, for each iteration, a model of the pulsating secondary component is subtracted from the pulsation light curve, the modes of the primary star fitted to the residuals and vice versa. This separate fitting and subtraction from the pulsation light curve is repeated an arbitrary five times.

The parameters for the phase dependent amplitudes are given in Table 4. In a circularized orbit, the expected phase difference between primary and secondary eclipse is equal to 0.5 $\frac{\text{rad}}{2\pi}$. For M_2, the difference between the phase of the minimum for the primary and secondary follows this expectation within 1σ. The resulting model has a total of 88 significant frequencies, 46 of which show amplitudes higher than 165 ppm and are specified in Table 5. The latter split in 32 assigned to the secondary and 14 assigned to the primary component. Therefore, this model has 20 low amplitude frequencies less than M_1, which has 108 significant frequencies and 45 with amplitudes higher than 165 ppm. We find similar combinations as for M_1 (see Table 5). The designation to a component is certainly not foolproof, especially for lower amplitude modes, but should be plausible for higher amplitude modes ($A \gtrsim 500$ ppm). Indeed, it is a reassuring sign that F5, F6 and F7 all point to the secondary component as their parent frequencies F2 and F4. This relationship does not hold for all frequencies with amplitudes $\lesssim 500$ ppm, however. Similar to the model M_1, M_2 shows 18 fully independent frequencies that coincide. We find that the frequencies in Table 5 and Table 3 resemble each other very well, apart from the amplitude. The latter is expected from the discussion in Appendix C. Table B.2 presents all frequencies in the model, independent of amplitude.

5.4. Model Comparison

Model M_2 with phase dependent amplitude, defined in equation (2) results in an amplitude spectrum that shows frequencies at $\pm i f_\mathrm{orb}$ where i is an integer. Using the resulting frequencies from the modelling of classical linear modes M_1, we indeed retrieve similar results. For F1, we find frequencies corresponding to $i \in [-3, -1, 1, 2, 3, 4, 5, 6, 7]$ and for F2 they correspond to $i \in [-2 - 1, 1, 2, 3, 4]$. If the splitting of a pulsation mode is due to tidal perturbation, the integers should follow $|i| \leq l$ (Smeyers 2005). This would lead to F1 being a $l = 5$ mode (if F1 $+2 f_\mathrm{orb}$ would be the parent frequency) and F2 being a $l = 3$ or $l = 4$ mode. If this was indeed the case, it would be highly unlikely to see them in photometry due to cancellation effects (Aerts et al. 2010).

Amplitude modulation due to arrival time delays is an additional process that would split the pulsating frequency in the amplitude spectrum (Shibahashi & Kurtz 2012). Using the values of Table 1, we derive the value $\alpha = 0.0092$ resulting in an relative amplitude of the first side peaks of $\frac{\alpha}{2} = 0.0042$ (according to equations (11) and (25) of Shibahashi & Kurtz (2012) and higher order side peaks would have even lower amplitudes rendering it impossible to provide such a rich frequency spectrum from this effect. Furthermore, this effect is significantly smaller than the expected amplitudes for M_2 (see also Appendix C).

We therefore deduce that the splitting is at least partly caused by phase dependent amplitude variations. At the present time we cannot decide if these variations have the form given in equation (2).

Table 5. The identified frequencies using superposition of modes with phase dependent amplitude and their corresponding amplitudes and phases.

Designation in model M_2	M_1	f (d^{-1})	A (ppm)	ϕ ($\frac{rad}{2\pi}$)	C
$\tilde{F}1$	F1	11.070408(5)	1766(14)	0.861(6)	S
$\tilde{F}2$	F2	11.624950(6)	1722(15)	0.891(7)	S
$\tilde{F}3$	F3	12.795295(7)	1533(14)	0.841(9)	S
$\tilde{F}4$	F4	20.122577(10)	916(14)	0.635(12)	S
$\tilde{F}5=\tilde{F}4-2f_{orb}$	F5	18.924939(11)	851(14)	0.629(13)	S
$\tilde{F}6=\tilde{F}2-2f_{orb}$	F7	10.427267(13)	736(14)	0.560(15)	S
$\tilde{F}7=\tilde{F}2+2f_{orb}$	F6	12.822557(14)	690(15)	0.006(18)	S
$\tilde{F}8$	F8	25.636124(15)	604(14)	0.001(18)	S
$\tilde{F}9$	F9	0.385008(17)	553(14)	0.821(20)	P
$\tilde{F}10=\tilde{F}9+\tilde{F}2$	F11	12.004933(28)	372(15)	0.09(4)	S
$\tilde{F}11$	F15	26.474945(26)	358(15)	0.44(3)	P
$\tilde{F}12$	F12	21.064362(26)	355(14)	0.95(3)	S
$\tilde{F}13$	F13	24.231101(27)	343(14)	0.70(3)	P
$\tilde{F}14=2\tilde{F}3$	F16	25.588559(29)	327(14)	0.38(3)	P
$\tilde{F}15$	F17	26.024095(29)	325(14)	0.05(3)	S
$\tilde{F}16$	F20	18.78986(3)	315(14)	0.98(4)	S
$\tilde{F}17$	F10	1.20448(4)	311(15)	0.78(5)	S
$\tilde{F}18$	F19	21.15649(3)	303(14)	0.76(4)	S
$\tilde{F}19=\tilde{F}11-3f_{orb}$	F25	25.27767(3)	301(15)	0.34(4)	P
$\tilde{F}20=\tilde{F}13-2f_{orb}$	F18	23.03411(3)	296(14)	0.61(4)	S
$\tilde{F}21$	F21	26.31002(3)	285(14)	0.42(4)	S
$\tilde{F}22$	F22	25.36352(3)	277(14)	0.79(4)	S
$\tilde{F}23=2\tilde{F}13-\tilde{F}18$	F24	27.30485(4)	271(14)	0.80(4)	S
$\tilde{F}24=2\tilde{F}16-\tilde{F}8$	F27	11.94672(3)	270(14)	0.10(4)	P
$\tilde{F}25=\tilde{F}15+2f_{orb}$	F23	27.22180(4)	257(14)	0.95(4)	S
$\tilde{F}26=\tilde{F}2-f_{orb}$	F14	11.02619(4)	257(14)	0.61(4)	S
$\tilde{F}27$	F28	19.80505(4)	254(14)	0.52(4)	P
$\tilde{F}28$	F32	30.10362(4)	250(15)	0.36(5)	P
$\tilde{F}29=\tilde{F}22-2f_{orb}$	F26	24.43831(4)	241(14)	0.29(4)	S
$\tilde{F}30$	F31	26.93403(4)	216(14)	0.28(5)	S
$\tilde{F}31$	F36	25.79580(4)	209(14)	0.32(5)	S
$\tilde{F}32=\tilde{F}29-\tilde{F}24$	F33	12.49488(5)	205(14)	0.81(6)	P
$\tilde{F}33=\tilde{F}31-2f_{orb}$	F41	24.59732(5)	202(14)	0.24(5)	S
$\tilde{F}34$	F38	29.67910(5)	198(15)	0.31(6)	P
$\tilde{F}35=\tilde{F}29-2\tilde{F}2$	F42	1.18997(6)	196(15)	1.00(8)	S
$\tilde{F}36=2\tilde{F}8-\tilde{F}23$	F39	23.96719(5)	192(14)	0.86(6)	S
$\tilde{F}37=\tilde{F}36-\tilde{F}24$	F37	12.01960(5)	192(14)	0.16(7)	S
$\tilde{F}38=2\tilde{F}29-\tilde{F}16$	F43	30.09070(5)	188(15)	0.85(7)	P
$\tilde{F}39=\tilde{F}23-2f_{orb}$	F35	26.10774(5)	187(14)	0.91(6)	S
$\tilde{F}40=\tilde{F}32-f_{orb}$	F34	11.89424(5)	186(14)	0.90(6)	P
$\tilde{F}41=2\tilde{F}17$	F29	2.40322(5)	180(14)	0.46(6)	S
$\tilde{F}42=\tilde{F}36+4f_{orb}$	F40	26.36587(5)	180(14)	0.78(6)	P
$\tilde{F}43=2\tilde{F}35+\tilde{F}41$	F45	4.78393(5)	177(14)	0.59(6)	S
$\tilde{F}44=2\tilde{F}24-\tilde{F}37$	F46	11.87541(5)	173(14)	0.96(6)	S
$\tilde{F}45=\tilde{F}27-2f_{orb}$	F49	18.60774(5)	171(14)	0.48(6)	S
$\tilde{F}46=\tilde{F}1+2f_{orb}$	F30	12.86735(6)	167(14)	0.84(7)	P

Notes. The values in parentheses give the 1σ uncertainty as a combination of the values reported by the least square algorithm and the standard error estimates formulated by Montgomery & O'Donoghue (1999). f_{orb} is the orbital frequency. C is a shortcut for Component and denotes either the primary (P) or secondary (S) whichever was chosen according to the test statistics. Further possible combinations are: $\tilde{F}23=2\tilde{F}19-2\tilde{F}2=2\tilde{F}11-2\tilde{F}7$; $\tilde{F}26=2\tilde{F}8-2\tilde{F}4$; $\tilde{F}37=2\tilde{F}12-\tilde{F}28=\tilde{F}3-2\tilde{F}9$; $\tilde{F}42=2\tilde{F}3+2\tilde{F}9$; $\tilde{F}43=\tilde{F}8-2\tilde{F}6=4\tilde{F}17$; $\tilde{F}46=2\tilde{F}24-\tilde{F}26$

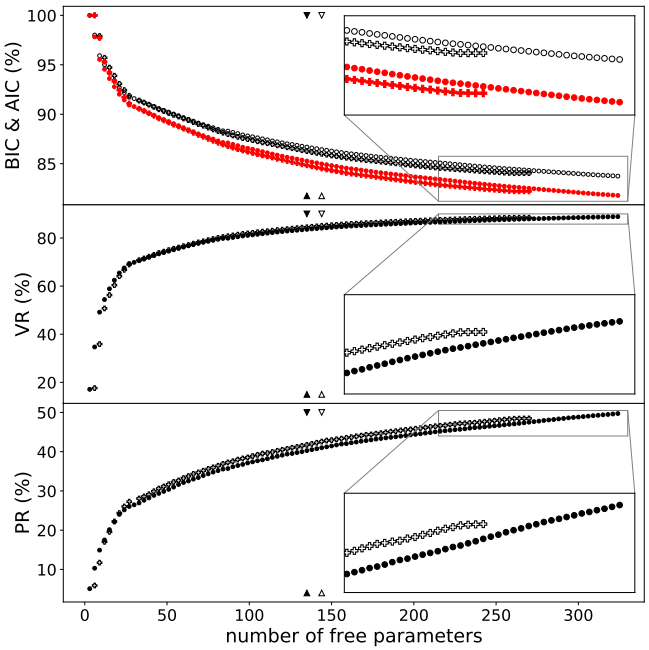

Fig. 8. The four different test statistics for our models M_1 and M_2 as a function of the number of free parameters. Circles denote the model M_1 while pluses denote model M_2. The filled (open) triangles mark the number of free parameters using only the frequencies with amplitude higher than 165 ppm for M_1 (M_2). Top panel: AIC and BIC, where black open symbols correspond to the BIC and red filled symbols to the AIC. These statistics were calculated in respect to pulsation light curve. Middle panel: VR. Bottom panel: PR. All the insets show zoom-ins toward the areas concerning higher number of parameters.

This is further confirmed by the fact that model M_2 shows only frequencies corresponding to $i \in [1, 3]$ for F1 and $i \in [-3, -2, -1, 1, 2]$ for F2. These frequency multiplets are more plausible in the light of tidally perturbed modes (discussed in Section 6). Our results show that the side peaks corresponding to higher i in model M_1 most probably arise from the phase dependent amplitude due to binary eclipses and not, as would otherwise be expected, from the stellar pulsation signal itself.

Figure 8 shows the calculated model statistics, where the top panel compares the AIC and BIC for, the middle panel shows the VR and the lower panel shows the PR of both models. All statistics agree on the following: The model with phase dependent amplitudes M_2 describes the light curve better at a fixed number of degrees of freedoms (and therefore model frequencies). The additional frequencies in M_1 although improve this model further, outweighing the cost of additional free parameters for both the AIC and BIC. Using only the frequencies with amplitude higher than 165 ppm, all statistics agree that modes with phase dependent amplitude model the pulsation light curve of RS Cha more successfully than classical linear modes. Furthermore, the BIC and AIC discourages the use of the last three frequencies for M_2, which is not surprising, given their low amplitudes.

6. Evidence for Tidally Perturbed Modes

The theoretical works by Reyniers & Smeyers (2003a,b) and Smeyers (2005) discuss the effect of the equilibrium tide on linear, isentropic oscillations of a star in a circular orbit close binary system. The authors predict the presence of perturbed eigenmodes, solidifying themselves as multiplets spaced by (twice)

the orbital frequency. A pulsation mode of degree l splits into $l+1$ frequencies corresponding to $|\tilde{m}| = 0, 1, 2, \ldots, l$,[2] each of which will furthermore split into multiplets depending on their value of l and $|\tilde{m}|$ respectively. A summary of the theory was given by Balona (2018).

RS Cha is a circularized and synchronized (Alecian et al. 2005) binary system and is therefore a splendid specimen to test this theory according to which we would see multiple subsets of frequencies spaced by either once or twice the orbital frequency. Furthermore, the recognition of specific frequency patterns may allow the identification of pulsation modes. As discussed above and in Section 5.4, both, tidal perturbation and phase dependent amplitudes, lead to a similar signature in terms of inferred frequencies. It is therefore essential to disentangle the effect of the phase dependent amplitude before any discussion of the results in light of the theory by Reyniers & Smeyers (2003a,b).

Figure 9 shows all significant frequencies from model M_1 (black dots) and M_2 (colored crosses) above 8 d^{-1}modulo the orbital frequencies. It is clearly visible that multiple sets of frequencies are split by the orbital frequency. The top panel in Figure 9 shows the signatures expected from the theory of tidally perturbed pulsations taken from Smeyers (2005) and Balona (2018). These signatures can be identified several times in the bottom panel. We therefore see clear evidence for tidally perturbed modes in both components of RS Cha. In the following we will try to identify the modes according to their respective multiplets.

Modelling the light curve with a superposition of modes with phase dependent amplitude (model M_2) gives viable hints on the origin of a given frequency. Using this information we differentiate between three categories of evidence for tidally perturbed modes without any statistical justification:

- **strong evidence**
  A set of frequencies forms a multiplet as expected from the theory of tidal perturbations. All frequencies of this multiplet have been significant in both models M_1 and M_2 and all frequencies are assigned to the same component in model M_2.
- **moderate evidence**
  A set of frequencies forms a multiplet as expected from the theory of tidal perturbations. However, either the frequencies have not been significant in both models M_1 and M_2, or the frequencies have been assigned to different components in model M_2
- **weak evidence**
  A set of frequencies does not form a multiplet as expected by the theory of tidal perturbations. However, the frequencies are significant in either the model M_1 or M_2 and are split by the orbital frequency.

Starting from the frequency with the highest amplitude F1 (or $\tilde{F}1$) shows only **weak evidence**. Although there are multiple low amplitude frequencies spaced with the orbital frequency in model M_1, there are only three in model M_2 from which only F1 and F105 (or $\tilde{F}1$ and $\tilde{F}82$) are assigned to the secondary while F30 (or $\tilde{F}46$) is assigned to the primary. The signature does not resemble any expected from theory which makes an identification impossible.

[2] Here, $\tilde{m}$ refers to the azimuthal number in the system of spherical coordinates system where the polar axis aligns with the axis joining the center of mass of the two stars (Reyniers & Smeyers 2003b; Balona 2018). This is different from the standard azimuthal number m corresponding to the co-rotating coordinate system where the polar axis coincides with the orbital axis.

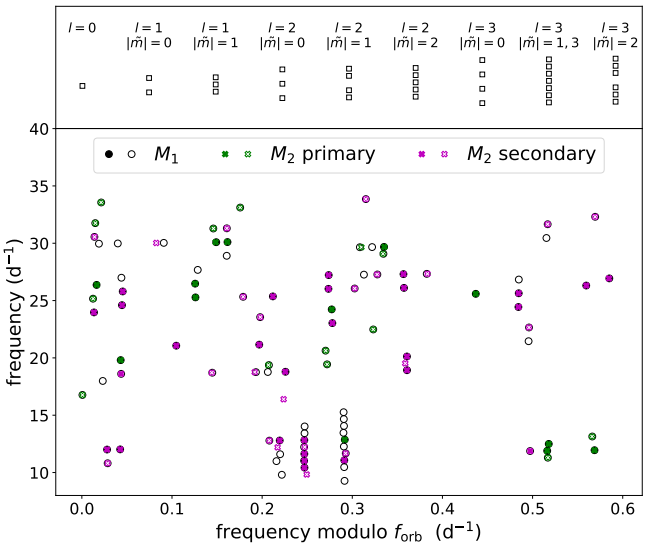

Fig. 9. Top panel: The signature of multiplets expected from the theory of of perturbed pulsation corresponding to different values of l and $|\tilde{m}|$. Multiplets are plotted according to the tables in Smeyers (2005) and Balona (2018). Bottom panel: All significant frequencies in both models M_1 and M_2 above 8 d^{-1}modulo the orbital frequency. Frequencies in model M_1 are shown as black circles were filled circles indicate the frequencies with amplitudes above 165 ppm and open circles frequencies below that amplitude level. Frequencies in model M_2 are shown as colored crosses: green crosses correspond to frequencies assigned to the primary component while magenta crosses correspond to frequencies assigned to the secondary component. Low amplitude modes are depicted as open crosses, as for frequencies from M_1. The frequencies are clearly split by the orbital frequencies and often reproduce signatures as expected from the theory.

F2 (or $\tilde{F}2$) shows **strong evidence** to be a $l = 2$, $|\tilde{m}| = 2$ mode. We find a set of five frequencies F7, F14, F2, F93, and F6 (or $\tilde{F}6$, $\tilde{F}26$, $\tilde{F}2$, $\tilde{F}88$, and $\tilde{F}7$) corresponding to F2 (or $\tilde{F}2$) $\pm i f_{\rm orb}$ with $i \in [-2, -1, 0, 1, 2]$ as would be expected for a mode of degree degree $l = 2$ and azimuthal number $|\tilde{m}| = 2$. All of these five frequencies are significant in both M_1 and M_2 and are assigned to the secondary component in model M_2.

As discussed in Section 5, F3 (or $\tilde{F}3$) has a frequency ($f = 12.795$ d^{-1}) similar to a $l = 2$ or 3 mode ($f = 12.81$ d^{-1}) reported by Böhm et al. (2009). We find only **weak evidence** for F3 to be a tidally perturbed mode, and none that would put it as an $l = 2$ or 3 mode. On the other hand, F6 (or $\tilde{F}7$) ($f = 12.822$ d^{-1}) is similarly close to the reported value from Böhm et al. (2009) and is part of the multiplets showing strong evidence to correspond to a $l = 2$ mode. With its amplitude of ≈ 750 ppm it is one of the most prominent frequencies in photometry and it might therefore be reasonable to expect it in spectroscopy as well.

F4 (or $\tilde{F}4$), together with F5 (or $\tilde{F}5$) show **strong evidence** to be a $l = 1$, $|\tilde{m}| = 0$ mode because both are assigned to the secondary component. $\tilde{F}86$ is only significant in model M_2 and shows a very low amplitude (≈ 40 ppm). As discussed in Section 5.4, both the AIC and the BIC discourage from including this frequency However, including $\tilde{F}86$ would lead to **moderate evidence** for this multiplet to stem from a $l = 1$, $|\tilde{m}| = 1$ mode.

Furthermore, we can identify a total of 25 cases which show evidence for tidally perturbed modes. These are given in Table 6. 12 of these 25 cases show strong evidence and can be attributed to a component of the binary. However, it occurs that similar to F4, some of this also show moderate evidence with the addition

Table 6. Evidence for tidally perturbed modes and corresponding mode identification.

M_1	M_2	l	$\|\tilde{m}\|$	evidence	C
F1 F30 F105	$\tilde{F}$1 $\tilde{F}$46 $\tilde{F}$82	-	-	weak	-
F2 F6 F7 F14 F93	$\tilde{F}$2 $\tilde{F}$6 $\tilde{F}$7 $\tilde{F}$26 $\tilde{F}$88	2	2	strong	S
F4 F5	$\tilde{F}$4 $\tilde{F}$5	1	0	strong	S
F4 F5	$\tilde{F}$4 $\tilde{F}$5 $\tilde{F}$86	1	1	moderate	S
F8 F26	$\tilde{F}$8 $\tilde{F}$29	1	0	strong	S
F8 F26 F854	$\tilde{F}$8 $\tilde{F}$29	2	0	weak	-
F11 F69	$\tilde{F}$10 $\tilde{F}$55	1	0	strong	S
F13 F18	$\tilde{F}$13 $\tilde{F}$20	1	0	moderate	-
F15 F25	$\tilde{F}$11 $\tilde{F}$19	1	0	strong	P
F15 F25 F94	$\tilde{F}$11 $\tilde{F}$19	2	0	weak	-
F17 F23	$\tilde{F}$15 $\tilde{F}$25	1	0	strong	S
F24 F35	$\tilde{F}$23 $\tilde{F}$39	1	0	strong	S
F27 F81	$\tilde{F}$24 $\tilde{F}$80	1	0	strong	P
F28 F49	$\tilde{F}$27 $\tilde{F}$45	1	0	moderate	-
F32 F57	$\tilde{F}$28 $\tilde{F}$51	1	0	moderate	-
F33 F34 F66	$\tilde{F}$32 $\tilde{F}$40 $\tilde{F}$60	1	1	strong	P
F36 F41	$\tilde{F}$31 $\tilde{F}$33	1	0	strong	S
F36 F41 F84	$\tilde{F}$31 $\tilde{F}$33	2	0	weak	-
F38 F56	$\tilde{F}$34 $\tilde{F}$59	-	-	weak	-
F39 F40 F61	$\tilde{F}$36 $\tilde{F}$42 $\tilde{F}$54	2	0	moderate	-
F43 F71	$\tilde{F}$38 $\tilde{F}$53	1	0	strong	P
F47 F50	$\tilde{F}$47 $\tilde{F}$49	1	0	moderate	-
F73 F74	$\tilde{F}$67	1	0	weak	-
F77 F107	$\tilde{F}$65	1	0	weak	-
F98 F101	$\tilde{F}$81 $\tilde{F}$83	1	0	strong	P

Notes. M_1 and M_2 correspond to the different models described in Section 5.2 and Section 5.3 respectively. l and $\tilde{m}$ correspond to the mode degree and azimuthal number as in Reyniers & Smeyers (2003b,a) and Smeyers (2005). C is a shortcut for component where P corresponds to the primary and S to the secondary. See the text for a description of the evidence.

of another frequency. According to the mode identification, both, the primary and secondary component seem to exhibit mostly dipole modes. We identify more $l = 1$, $\tilde{m} = 0$ modes of the secondary in the frequency range 25 $d^{-1}$to 27 d^{-1}than expected from theory. Currently, we have no explanation for that. Additional work is needed to verify the mode identification.

Radial pulsation modes are not split when transforming to a non rotating reference frame (i.e. the observers frame). Hence, they should appear without a side peak in the amplitude spectrum. Multiple single frequencies, significant in both M_1 and and M_2 are evident in Figure 9. However, since most of these are combination frequencies, identifying them as radial pulsation modes is dangerous. Some, for example F12, F19, F20, F21, F22, F55, and F89 are completely independent in both M_1 and M_2. Their existence has two possible explanations: (i), the amplitudes of the split frequencies are too low to be observed or (ii), they correspond to radial modes. For the high amplitude frequencies (F12, F19, F20, F21, F22), we would expect to be able to observe the split frequencies. Therefore, the identification of these modes as radial pulsation modes should be more reliable.

7. Conclusion

We presented the TESS photometric observations of RS Cha, a pre-main sequence binary system consisting of two δ Scuti stars that is circularized and synchronized. Approximately a third of the light curve was modelled with `PHOEBE` to remove the eclipsing binary signal from the light curve. Because the orbital parameters are well constrained (e.g. Alecian et al. 2005), we used a Nelder Mead optimization to derive a good model for light curve of the binary system. Some residuals at the time of primary and secondary eclipses were removed by fitting multiples of the orbital frequency to the phase folded residual.

The remaining residuals were used in the subsequent pulsation analysis. Because the most dominant frequencies in the amplitude spectrum show strong amplitude decreases during the time of secondary eclipses, we modelled the pulsation signal with two distinct sets of frequencies. The classical superposition of linear modes resulted in 108 frequencies, 45 of which have amplitudes higher than the expected noise level of the corresponding TESS observations (165 ppm). The second model included frequencies whose amplitude was modified by a negative Gaussian peak either during primary or secondary eclipse. We used different information criteria to assign each frequency to a component. This resulted in a total of 88 significant frequencies, 46 of which have amplitudes higher than 165 ppm.

We used the same information criteria to assess the goodness of fit for both models and found that the model with phase dependent amplitudes M_2 describes the light curve better for a given number of degrees of freedom, although the additional frequencies in the classical model M_1 lead to an improvement that outweighs the addition of the corresponding free parameters. These results suggests that indeed a model with phase dependent amplitudes is to be preferred to model the pulsational signal of the binary system RS Cha, but it is evident that the model chosen by us cannot be the final solution. Three distinct mechanisms lead to similar signals in the amplitude spectrum and therefore influence the extracted frequencies from a classical model of superposition of linear modes. These are: phase dependent amplitudes, tidally perturbed oscillations (Reyniers & Smeyers 2003a,b) and time delay effects (Shibahashi & Kurtz 2012). While time delay effects can be neglected given the orbital parameters of RS Cha, phase dependent amplitudes have an enormous effect on the observed frequencies. The information from the distinct models were used to interpret the results in terms of the theory of tidally perturbed modes according to Reyniers & Smeyers (2003a,b) and Smeyers (2005).

We found strong evidence for tidally perturbed modes and used patterns to identify pulsation modes from frequency multiplets. From this discussion, we find that both, the primary and secondary mainly pulsate in dipole modes with the addition of one strong quadrupole mode originating in the secondary component. The identification of this quintuplet of frequencies agrees with the mode identification based on spectroscopic time series performed by Böhm et al. (2009), although there is a small frequency offset of 1.05 time the Rayleigh limit, which we deem negligible. Additionally, multiple independent frequencies are observed that, in terms of the theory, should correspond to radial modes.

RS Cha is therefore the first pre-main sequence star that shows tidal effects on its pulsational properties and the first doubly pulsating pre-main sequence star observed with TESS. Such systems are invaluable for the understanding of pre-main sequence asteroseismology. Future efforts will go into the identification and analysis of comparable systems and hence into increasing the sample size. RS Cha is furthermore the first object in which multiple pulsation modes could be identified from tidally perturbed modes and should be an ideal specimen to further test the theory of tidally perturbed modes. Seismic modelling, to-

gether with a quantitative analysis of the theory by Reyniers & Smeyers (2003a,b) and Smeyers (2005) is therefore the subject of future work.

Although often overlooked, the pre-main sequence phase plays an important role in stellar evolution — for example the g-mode frequencies of main sequence stars are strongly influenced by neglecting its pre-main sequence evolution calculations (Aerts et al. 2018). Due to the binary nature of RS Cha, the masses and radii of the components are well known. These, together with assumptions of the same age and chemical composition deliver strong constraints for modelling of the stellar interia that allow far more insight than otherwise possible (Schmid & Aerts 2016). This work lays the ground stone for subsequent work hopefully delivering constraints on angular momentum transport during the pre-main sequence phase. Hence, RS Cha is an important system to enhance our knowledge of stellar structure and evolution in the years to come.

Acknowledgements. We thank Conny Aerts and Bert Pablo for fruitful discussions. The research leading to these results has received funding from the European Research Council (ERC) under the European Union's Horizon 2020 research and innovation programme (grant agreement No. 670519: MAMSIE). The TESS data presented in this paper were obtained from the Mikulski Archive for Space Telescopes (MAST) at the Space Telescope Science Institute (STScI). Funding for the TESS mission is provided by the NASA Explorer Program. STScI is operated by the Association of Universities for Research in Astronomy, Inc., under NASA contract NAS5-26555. Support for MAST for non-HST data is provided by the NASA Office of Space Science via grant NNX13AC07G and by other grants and contracts. This research has made use of the SIMBAD database, operated at CDS, Strasbourg, France; NASA's Astrophysics Data System; matplotlib, a Python library for publication quality graphics (Hunter 2007); SciPy (Virtanen et al. 2020); Astropy, a community-developed core Python package for Astronomy (Astropy Collaboration et al. 2018, 2013); NumPy (Van Der Walt et al. 2011); MESA SDK for Mac OS (Version 20.3.1) (Townsend 2020).

References

Adibekyan, V., Sousa, S. G., & Santos, N. C. 2018, in Asteroseismology and Exoplanets: Listening to the Stars and Searching for New Worlds, ed. T. L. Campante, N. C. Santos, & M. J. P. F. G. Monteiro, Vol. 49, 225
Aerts, C. 2020, arXiv e-prints, arXiv:1912.12300
Aerts, C., Christensen-Dalsgaard, J., & Kurtz, D. W. 2010, Asteroseismology (Springer)
Aerts, C., Molenberghs, G., Michielsen, M., et al. 2018, ApJS, 237, 15
Alecian, E., Catala, C., Goupil, M. J., Lebreton, Y., & Dupret, M. A. 2006, Mem. Soc. Astron. Italiana, 77, 93
Alecian, E., Catala, C., van't Veer-Menneret, C., Goupil, M. J., & Balona, L. 2005, A&A, 442, 993
Alecian, E., Goupil, M. J., Lebreton, Y., Dupret, M. A., & Catala, C. 2007a, A&A, 465, 241
Alecian, E., Lebreton, Y., Goupil, M. J., Dupret, M. A., & Catala, C. 2007b, A&A, 473, 181
Antoci, V., Cunha, M. S., Bowman, D. M., et al. 2019, MNRAS, 490, 4040
Astropy Collaboration, Price-Whelan, A. M., Sipőcz, B. M., et al. 2018, AJ, 156, 123
Astropy Collaboration, Robitaille, T. P., Tollerud, E. J., et al. 2013, A&A, 558, A33
Balona, L. A. 2018, MNRAS, 476, 4840
Barentsen, G., Hedges, C. L., De Mirand a Cardoso, J. V., et al. 2019, in American Astronomical Society Meeting Abstracts, Vol. 233, American Astronomical Society Meeting Abstracts #233, 109.08
Bedding, T. R., Murphy, S. J., Hey, D. R., et al. 2020, Nature, 581, 147
Böhm, T., Zima, W., Catala, C., et al. 2009, A&A, 497, 183
Bowman, D. M., Johnston, C., Tkachenko, A., et al. 2019, ApJ, 883, L26
Bowman, D. M. & Kurtz, D. W. 2018, MNRAS, 476, 3169
Breger, M., Stich, J., Garrido, R., et al. 1993, A&A, 271, 482
Buzasi, D. L., Bruntt, H., Bedding, T. R., et al. 2005, ApJ, 619, 1072
Chaplin, W. J. & Miglio, A. 2013, ARA&A, 51, 353
Clausen, J. V. & Nordstrom, B. 1980, A&A, 83, 339
Cousins, A. W. J. 1960, Monthly Notes of the Astronomical Society of South Africa, 19, 56
De Marco, O. & Izzard, R. G. 2017, Publications of the Astronomical Society of Australia, 34, e001
Degroote, P., Briquet, M., Catala, C., et al. 2009, A&A, 506, 111
Frémat, Y., Lampens, P., Alecian, E., et al. 2006, Mem. Soc. Astron. Italiana, 77, 521
Fuller, J. 2017, MNRAS, 472, 1538
García, R. A. & Ballot, J. 2019, Living Reviews in Solar Physics, 16, 4
Hambleton, K. M., Kurtz, D. W., Prša, A., et al. 2013, MNRAS, 434, 925
Handler, G., Kurtz, D. W., Rappaport, S. A., et al. 2020, Nature Astronomy [arXiv:2003.04071]
Horvat, M., Conroy, K. E., Pablo, H., et al. 2018, ApJS, 237, 26
Hunter, J. D. 2007, Computing In Science & Engineering, 9, 90
Iben, Icko, J. 1965, ApJ, 141, 993
Jerzykiewicz, M., Pigulski, A., Handler, G., et al. 2020, MNRAS[arXiv:2006.05178]
Jones, D., Conroy, K. E., Horvat, M., et al. 2019, arXiv e-prints, arXiv:1912.09474
Koch, D. G., Borucki, W. J., Basri, G., et al. 2010, ApJ, 713, L79
Kurtz, D. W., Handler, G., Rappaport, S. A., et al. 2020, MNRAS, 494, 5118
Kuschnig, R., Weiss, W. W., Gruber, R., Bely, P. Y., & Jenkner, H. 1997, A&A, 328, 544
Lee, J. W., Hong, K., Kim, S.-L., & Koo, J.-R. 2016, MNRAS, 460, 4220
Lomb, N. R. 1976, Ap&SS, 39, 447
Luhman, K. L. & Steeghs, D. 2004, ApJ, 609, 917
Lundkvist, M. S., Huber, D., Aguirre, V. S., & Chaplin, W. J. 2018, Characterizing Host Stars Using Asteroseismology, ed. H. J. Deeg & J. A. Belmonte (Cham: Springer International Publishing), 1655–1678
Maceroni, C., Lehmann, H., da Silva, R., et al. 2014, A&A, 563, A59
Mayer, P. & Hanna, M. A. M. 1991, Bulletin of the Astronomical Institutes of Czechoslovakia, 42, 98
McInally, C. J. & Austin, R. D. 1977, Information Bulletin on Variable Stars, 1334, 1
Montgomery, M. H. & O'Donoghue, D. 1999, Delta Scuti Star Newsletter, 13, 28
Morris, R. L., Twicken, J. D., Smith, J. C., et al. 2017, Kepler Data Processing Handbook: Photometric Analysis, Kepler Science Document
Müllner, M. 2020, MarcoMuellner/SMURFS 1.1.3
Nelder, J. A. & Mead, R. 1965, The Computer Journal, 7, 308
Pamyatnykh, A. A. 2000, Astronomical Society of the Pacific Conference Series, Vol. 210, Pulsational Instability Domain of δ Scuti Variables, ed. M. Breger & M. Montgomery, 215
Paxton, B., Bildsten, L., Dotter, A., et al. 2011, ApJS, 192, 3
Paxton, B., Cantiello, M., Arras, P., et al. 2013, ApJS, 208, 4
Paxton, B., Marchant, P., Schwab, J., et al. 2015, ApJS, 220, 15
Paxton, B., Schwab, J., Bauer, E. B., et al. 2018, ApJS, 234, 34
Paxton, B., Smolec, R., Schwab, J., et al. 2019, ApJS, 243, 10
Polfliet, R. & Smeyers, P. 1990, A&A, 237, 110
Prša, A., Conroy, K. E., Horvat, M., et al. 2016, ApJS, 227, 29
Prša, A. & Zwitter, T. 2005, ApJ, 628, 426
Reyniers, K. & Smeyers, P. 2003a, A&A, 409, 677
Reyniers, K. & Smeyers, P. 2003b, A&A, 404, 1051
Ribas, I., Jordi, C., Torra, J., & Giménez, Á. 2000, MNRAS, 313, 99
Ricker, G. R., Winn, J. N., Vanderspek, R., et al. 2015, Journal of Astronomical Telescopes, Instruments, and Systems, 1, 014003
Rodríguez, E. & Breger, M. 2001, A&A, 366, 178
Savitzky, A. & Golay, M. J. E. 1964, Analytical Chemistry, 36, 1627
Scargle, J. D. 1982, ApJ, 263, 835
Schmid, V. S. & Aerts, C. 2016, A&A, 592, A116
Shibahashi, H. & Kurtz, D. W. 2012, MNRAS, 422, 738
Smeyers, P. 2005, Astronomical Society of the Pacific Conference Series, Vol. 333, Dynamic theory of tides in close binaries, and effects on the apsidal motion and stellar oscillations, ed. A. Claret, A. Giménez, & J. P. Zahn, 39
Southworth, J., Bowman, D. M., Tkachenko, A., & Pavlovski, K. 2020, MNRAS, 497, L19
Spendley, W., Hext, G. R., & Himsworth, F. R. 1962, Technometrics, 4, 441
Stellingwerf, R. F. 1978, ApJ, 224, 953
Strohmeier, W. 1964, Information Bulletin on Variable Stars, 55, 1
Townsend, R. 2020, MESA SDK for Mac OS
Van Der Walt, S., Colbert, S. C., & Varoquaux, G. 2011, Computing in Science & Engineering, 13, 22
Verma, K., Antia, H. M., Basu, S., & Mazumdar, A. 2014, ApJ, 794, 114
Verma, K., Raodeo, K., Antia, H. M., et al. 2017, ApJ, 837, 47
Verma, K., Raodeo, K., Basu, S., et al. 2019, MNRAS, 483, 4678
Verma, K. & Silva Aguirre, V. 2019, MNRAS, 489, 1850
Virtanen, P., Gommers, R., Oliphant, T. E., et al. 2020, Nature Methods, 17, 261
Welsh, W. F., Orosz, J. A., Aerts, C., et al. 2011, ApJS, 197, 4
Woollands, R. M., Pollard, K. R., Ramm, D. J., Wright, D. J., & Böhm, T. 2013, MNRAS, 432, 327
Zahn, J. P. 1977, A&A, 500, 121
Zwintz, K. 2017, in European Physical Journal Web of Conferences, Vol. 160, European Physical Journal Web of Conferences, 03002
Zwintz, K. 2019, Frontiers in Astronomy and Space Sciences, 6, 68
Zwintz, K., Fossati, L., Ryabchikova, T., et al. 2014, Science, 345, 550

Appendix A: Nelder-Mead Method

The Nelder-Mead method, introduced by Nelder & Mead (1965) is a simplex method for function minimization based on a method developed by Spendley et al. (1962). The algorithm we implemented is slightly different from the original Nelder-Mead method and takes the following steps:

1. An initial simplex of $n + 1$ vertices is generated. Here n is the number of free parameters. Each vertex is a point $x_i \in \mathbb{R}^n$ together with a function value $f(x_i)$ where $f : \mathbb{R}^n \to \mathbb{R}$ is the function to minimize. In our case, f is the χ^2 of the residuals, the binary model flux $F_{\rm model}$ subtracted from the light curve flux $F_{\rm observed}$,

$$\chi^2 = \sum_i (F_{{\rm observed},i} - F_{{\rm model},i})^2 \ . \tag{A.1}$$

   The simplex is then sorted such that

$$f(x_1) \leq f(x_2) \leq \cdots \leq f(x_{n+1}) \tag{A.2}$$

   and the simplex centroid $x_{\rm c}$ for all but the worst vertex is calculated:

$$x_{\rm c} = \frac{1}{n} \sum_{k=1}^{n} x_k \ . \tag{A.3}$$

   At this point the iterations begin.
2. Since x_{n+1} is the worst point in the simplex, we might expect that the point resulting in a reflection on the centroid is better. Therefore, the reflected point $x_{\rm r}$ is calculated:

$$x_{\rm r} = (1 + \alpha)x_{\rm c} - \alpha x_{n+1} \ . \tag{A.4}$$

   Here $\alpha > 0$ is the reflection coefficient. If the function value of $x_{\rm r}$ fulfills $f(x_1) \leq f(x_{\rm r}) < f(x_n)$, the vertex x_{n+1} is replaced by the reflected point and the iteration ends.
3. If the reflected point is a new minimum, hence $f(x_{\rm r}) < f(x_1)$, there might be an even better point further in that direction. Thus, the expanded point $x_{\rm e}$ is calculated:

$$x_{\rm e} = \gamma x_{\rm r} + (1 - \gamma)x_{\rm c} \ . \tag{A.5}$$

   Here, $\gamma > 1$ is the expansion coefficient. The worst point in the simplex is then replaced by either the reflected point or the expanded point, whichever has the lower function value, and the iteration ends.
4. If the reflected point is worse than x_n, we might expect that a vertex better than x_{n+1} lies inside the simplex. Therefore the contracted point $x_{\rm t}$ is calculated:

$$x_{\rm t} = \beta x_{n+1} + (1 - \beta)x_{\rm c} \ . \tag{A.6}$$

   Here, β is the contraction coefficient that lies between 0 and 1. If the contracted point is better than the worst point, then the latter is replaced by the contracted point and the iteration ends. Otherwise, the iteration failed. In such a case, the size of the simplex is reduced by replacing all vertices x_i other than the best by

$$x_i = (1 - \rho)x_1 + \rho x_i \ . \tag{A.7}$$

   Here, ρ is the shrink coefficient.

Usual values for the coefficients are $\alpha = 1$, $\gamma = 2$, $\beta = 0.5$ and $\rho = 0.5$. The Nelder-Mead method might be caught in a local minimum. To maximize the chance of escaping such a situation, one can use more aggressive coefficients, $\alpha = 2$, $\gamma = 2$, $\beta = 0.95$ and $\rho = 0.95$. With such coefficients, the reflected and expanded point lies farther away from the initial simplex, and the size of the simplex is reduced slower, both giving more opportunities to withstand a local minimum.

There are multiple conditions one could apply to terminate the iteration. This includes testing the size of the simplex, the standard deviation of the function values in the simplex, or a pre-specified number of iterations. Experiments show, that the algorithm usually takes 200 n iteration to converge toward a final point [3], although there is no guarantee that this point is a global minimum! We find that 1000 iteration suffice, meaning that the best point has not changed for 200+ iterations.

As for the termination, there are multiple options on how to build the initial simplex. It should be general enough to allow the algorithm to explore all directions, but also small enough in order not to loose multiple iterations of contraction without improving the best point. We take a given starting point $x_{\rm s}$ and create n additional points by moving a small value δ in either direction of the parameter space

$$x_j = x_{\rm s} + \delta_j e_j \qquad \text{for } \ j = 1, \cdots, n \ . \tag{A.8}$$

Here, δ_j is a small number with $|\delta_j| \leq 0.05$ and e_j is the unit vector in direction j of our parameter space.

Appendix B: Frequency Tables

[3] `https://www.scilab.org/sites/default/files/neldermead.pdf`

Table B.1. The full list of identified frequencies using superposition of linear modes and their corresponding amplitudes and phases.

Designation	Frequency (d^{-1})	Amplitude (ppm)	Phase ($\frac{rad}{2\pi}$)	Designation	Frequency (d^{-1})	Amplitude (ppm)	Phase ($\frac{rad}{2\pi}$)
F1	11.070396(6)	1671(14)	0.881(6)	F55	27.33067(7)	131(14)	0.14(8)
F2	11.624913(6)	1644(14)	0.951(7)	F56 = F38$-f_{orb}$	29.07919(7)	131(14)	0.42(8)
F3	12.795260(7)	1450(14)	0.898(10)	F57 = F32+2f_{orb}	31.30082(7)	130(14)	0.60(8)
F4	20.122555(10)	909(14)	0.671(12)	F58	25.33049(7)	129(14)	0.09(8)
F5 = F4$-2f_{orb}$	18.924924(11)	852(14)	0.654(12)	F59 = F42+F42	2.38469(8)	129(14)	0.21(10)
F6 = F2+2f_{orb}	12.822585(13)	751(14)	0.955(16)	F60 = 2F59+F56	33.85044(7)	126(14)	0.42(8)
F7 = F2$-2f_{orb}$	10.427359(13)	689(14)	0.416(16)	F61 = F39+2f_{orb}	25.16393(7)	123(14)	0.85(9)
F8	25.636172(16)	586(14)	0.923(18)	F62 = 2F44+F23	29.65189(10)	122(15)	0.12(14)
F9	0.384953(17)	526(14)	0.911(20)	F63 = F39+4f_{orb}	23.55283(8)	121(14)	0.14(9)
F10	1.20499(9)	355(6)	0.93(15)	F64 = 2F9+F25	26.05303(8)	120(14)	0.82(9)
F11 = F2+F9	12.004905(29)	353(14)	0.14(4)	F65 = F24$-$2F48	22.48058(8)	120(14)	0.43(9)
F12	21.064357(27)	336(14)	0.96(3)	F66 = F33$-2f_{orb}$	11.29616(8)	120(14)	0.02(9)
F13	24.231017(27)	333(14)	0.84(3)	F67 = F3$-3f_{orb}$	10.99512(8)	119(14)	0.14(9)
F14 = F2$-f_{orb}$	11.025846(28)	331(14)	0.17(3)	F68 = F38$-$F29	27.27591(9)	119(14)	0.14(12)
F15	26.474933(29)	320(14)	0.46(3)	F69 = F11$-2f_{orb}$	10.80785(8)	118(14)	0.62(9)
F16 = 2F3	25.58853(3)	307(14)	0.43(4)	F70 = F47$-3f_{orb}$	29.96127(8)	115(14)	0.04(10)
F17	26.02396(3)	304(14)	0.26(4)	F71 = F43+2f_{orb}	31.28586(8)	115(14)	0.45(10)
F18 = F13$-2f_{orb}$	23.03406(3)	302(14)	0.70(4)	F72 = F1+4f_{orb}	13.46483(8)	112(14)	0.74(10)
F19	21.15642(3)	296(14)	0.86(4)	F73 = F30+F20	31.65674(8)	112(14)	0.04(10)
F20	18.79018(3)	283(14)	0.45(4)	F74 = F73$-2f_{orb}$	30.45769(8)	111(14)	0.32(10)
F21	26.30992(3)	278(14)	0.58(4)	F75 = F53+F49	18.70894(8)	110(14)	0.78(10)
F22	25.36344(3)	276(14)	0.93(4)	F76 = F68$-$F35	1.16366(9)	109(15)	0.67(11)
F23 = F17+2f_{orb}	27.22191(4)	267(14)	0.76(4)	F77 = F14+F2	22.65336(8)	108(14)	0.93(10)
F24 = 2F13$-$F19	27.30487(4)	265(14)	0.75(4)	F78 = F19$-4f_{orb}$	18.75736(10)	107(15)	0.61(14)
F25 = F15$-2f_{orb}$	25.27759(4)	261(14)	0.48(4)	F79 = F1+5f_{orb}	14.06425(8)	107(14)	0.49(10)
F26 = F8$-2f_{orb}$	24.43814(4)	259(14)	0.56(4)	F80 = 2F23$-$2F1	32.30832(8)	106(14)	0.66(10)
F27 = 2F20$-$F8	11.94680(4)	255(14)	0.99(4)	F81 = F27+2f_{orb}	13.14202(9)	105(14)	0.88(10)
F28	19.80501(4)	235(14)	0.59(4)	F82 = F1$-f_{orb}$	10.47140(9)	104(14)	0.98(10)
F29 = 2F10	2.40437(15)	228(10)	0.53(25)	F83 = F65+F1	33.55688(9)	102(14)	0.41(10)
F30 = F1+3f_{orb}	12.86744(4)	226(14)	0.68(5)	F84 = F27+2f_{orb}	26.99199(9)	101(14)	0.73(11)
F31 = F10+2F30	26.93439(4)	213(14)	0.69(5)	F85 = F2+3f_{orb}	13.42164(9)	99(14)	0.27(11)
F32	30.10391(5)	203(14)	0.89(6)	F86 = F2+4f_{orb}	14.02060(9)	99(14)	0.75(11)
F33 = F26$-$F27	12.49486(5)	195(14)	0.84(5)	F87 = 2F48+F61	29.98219(10)	99(14)	0.55(12)
F34 = F33$-f_{orb}$	11.89432(5)	193(14)	0.79(6)	F88 = F1$-3f_{orb}$	9.27411(10)	96(14)	0.87(11)
F35 = F24$-2f_{orb}$	26.10775(5)	190(14)	0.90(6)	F89	33.11220(10)	96(14)	0.25(11)
F36	25.79572(5)	188(14)	0.45(6)	F90 = F63$-$F45	18.77054(12)	95(15)	0.36(16)
F37 = F3$-$2F9	12.01945(6)	184(14)	0.41(7)	F91 = F32$-2f_{orb}$	28.90534(10)	95(14)	0.49(11)
F38	29.67863(6)	184(14)	0.11(8)	F92 = F1+6f_{orb}	14.66291(10)	94(14)	0.59(11)
F39 = 2F8$-$F24	23.96734(5)	182(14)	0.62(6)	F93 = F2+f_{orb}	12.22351(10)	94(14)	0.61(12)
F40 = 2F3+2F9	26.36555(5)	182(14)	0.31(6)	F94 = F15+2f_{orb}	27.67549(10)	94(14)	0.65(11)
F41 = F36$-2f_{orb}$	24.59721(5)	180(14)	0.41(6)	F95 = F90+f_{orb}	19.37061(10)	93(14)	0.17(11)
F42 = F26$-$2F2	1.19073(9)	179(18)	0.75(14)	F96 = F68+4f_{orb}	29.66546(14)	93(14)	0.01(20)
F43 = 2F29+F25	30.09140(6)	178(14)	0.69(7)	F97 = 2F48+F27	16.76834(10)	93(14)	0.51(11)
F44 = 2F6$-$F26	1.21202(16)	175(6)	0.81(25)	F98 = F74$-$F14	19.43512(10)	92(14)	0.54(12)
F45 = F8$-$2F7	4.78401(5)	167(14)	0.45(6)	F99 = F3$-5f_{orb}$	9.80338(10)	92(14)	0.95(12)
F46 = 2F27$-$F37	11.87532(6)	161(14)	0.10(7)	F100 = F62+F9	30.03321(10)	91(14)	0.30(12)
F47 = F28+F27	31.75374(6)	159(14)	0.77(7)	F101 = F98+2f_{orb}	20.63114(10)	90(14)	0.70(12)
F48 = 2F10	2.40982(22)	157(10)	0.0(4)	F102 = F1+7f_{orb}	15.26153(10)	90(14)	0.58(12)
F49 = F28$-2f_{orb}$	18.60787(6)	156(14)	0.26(7)	F103 = F62$-4f_{orb}$	27.26100(12)	86(14)	0.43(14)
F50 = F47$-2f_{orb}$	30.55512(6)	154(14)	0.41(7)	F104 = F59+F42	3.58133(11)	84(14)	0.32(12)
F51 = F1+2f_{orb}	12.26757(6)	153(14)	0.60(7)	F105 = F1+f_{orb}	11.67081(11)	83(14)	0.73(13)
F52 = F3$-2f_{orb}$	11.59805(6)	150(14)	0.16(7)	F106 = F103$-$F88	17.98861(11)	82(14)	0.24(13)
F53 = 2F30$-$F8	0.10162(6)	144(14)	0.94(7)	F107 = F77$-4f_{orb}$	21.45520(11)	81(14)	0.74(13)
F54 = F8+2f_{orb}	26.83395(7)	136(14)	0.67(8)	F108 = F76+F2	12.78379(13)	79(14)	0.45(18)

Notes. The values in parentheses give the 1σ uncertainty as a combination of the values reported by the least square algorithm and the standard error estimates formulated by Montgomery & O'Donoghue (1999). f_{orb} is the orbital frequency.

Table B.2. The full list of identified frequencies using superposition of modes with phase dependent amplitude and their corresponding amplitudes and phases.

Designation	Frequency (d^{-1})	Amplitude (ppm)	Phase ($\frac{rad}{2\pi}$)	C	Designation	Frequency (d^{-1})	Amplitude (ppm)	Phase ($\frac{rad}{2\pi}$)	C
$\tilde{F}1$	11.070408(5)	1766(14)	0.861(6)	S	$\tilde{F}45 = \tilde{F}27-2f_{orb}$	18.60774(5)	171(14)	0.48(6)	S
$\tilde{F}2$	11.624950(6)	1722(15)	0.891(7)	S	$\tilde{F}46 = \tilde{F}1+2f_{orb}$	12.86735(6)	167(14)	0.84(7)	P
$\tilde{F}3$	12.795295(7)	1533(14)	0.841(9)	S	$\tilde{F}47 = \tilde{F}27+\tilde{F}24$	31.75390(6)	163(14)	0.51(7)	P
$\tilde{F}4$	20.122577(10)	916(14)	0.635(12)	S	$\tilde{F}48 = 2\tilde{F}46-\tilde{F}8$	0.10157(6)	152(14)	0.02(7)	S
$\tilde{F}5 = \tilde{F}4-2f_{orb}$	18.924939(11)	851(14)	0.629(13)	S	$\tilde{F}49 = \tilde{F}47-2f_{orb}$	30.55527(6)	151(14)	0.17(7)	S
$\tilde{F}6 = \tilde{F}2-2f_{orb}$	10.427267(13)	736(14)	0.560(15)	S	$\tilde{F}50 = \tilde{F}35+\tilde{F}35$	2.38468(6)	151(14)	0.22(8)	S
$\tilde{F}7 = \tilde{F}2+2f_{orb}$	12.822557(14)	690(15)	0.006(18)	S	$\tilde{F}51 = \tilde{F}28+2f_{orb}$	31.30091(6)	150(14)	0.47(7)	S
$\tilde{F}8$	25.636124(15)	604(14)	0.001(18)	S	$\tilde{F}52$	27.33145(7)	135(14)	0.86(8)	S
$\tilde{F}9$	0.385008(17)	553(14)	0.821(20)	P	$\tilde{F}53 = \tilde{F}38+2f_{orb}$	31.28600(7)	134(14)	0.22(8)	P
$\tilde{F}10 = \tilde{F}9+\tilde{F}2$	12.004933(28)	372(15)	0.09(4)	S	$\tilde{F}54 = \tilde{F}36+2f_{orb}$	25.16413(7)	134(14)	0.52(8)	P
$\tilde{F}11$	26.474945(26)	358(15)	0.44(3)	P	$\tilde{F}55 = \tilde{F}10-2f_{orb}$	10.80786(7)	134(14)	0.61(8)	S
$\tilde{F}12$	21.064362(26)	355(14)	0.95(3)	S	$\tilde{F}56 = \tilde{F}41 -\tilde{F}35$	1.21482(7)	133(14)	0.21(8)	P
$\tilde{F}13$	24.231101(27)	343(14)	0.70(3)	P	$\tilde{F}57 = \tilde{F}28-2\tilde{F}50$	25.33052(7)	132(14)	0.05(8)	S
$\tilde{F}14 = \tilde{F}3+\tilde{F}3$	25.588559(29)	327(14)	0.38(3)	P	$\tilde{F}58 = 2\tilde{F}56+\tilde{F}25$	29.653587)	131(14)	0.36(9)	P
$\tilde{F}15$	26.024095(29)	325(14)	0.05(3)	S	$\tilde{F}59 = \tilde{F}34-f_{orb}$	29.07868(7)	129(14)	0.26(9)	P
$\tilde{F}16$	18.78986(3)	315(14)	0.98(4)	S	$\tilde{F}60 = \tilde{F}32-2f_{orb}$	11.29632(7)	128(14)	0.75(9)	P
$\tilde{F}17$	1.20448(4)	311(15)	0.78(5)	S	$\tilde{F}61 = 2\tilde{F}50+\tilde{F}59$	33.85039(7)	127(14)	0.50(9)	S
$\tilde{F}18$	21.15649(3)	303(14)	0.76(4)	S	$\tilde{F}62 = 2\tilde{F}2-2\tilde{F}9$	22.48058(7)	127(14)	0.43(9)	P
$\tilde{F}19 = \tilde{F}11-3f_{orb}$	25.27767(3)	301(15)	0.34(4)	P	$\tilde{F}63 = \tilde{F}18+4f_{orb}$	23.55301(7)	126(14)	0.85(9)	S
$\tilde{F}20 = \tilde{F}13-2f_{orb}$	23.03411(3)	296(14)	0.61(4)	S	$\tilde{F}64 = 2\tilde{F}9+\tilde{F}19$	26.05306(8)	123(14)	0.77(9)	S
$\tilde{F}21$	26.31002(3)	285(14)	0.42(4)	S	$\tilde{F}65 = \tilde{F}26+\tilde{F}2$	22.65334(8)	122(14)	0.97(9)	S
$\tilde{F}22$	25.36352(3)	277(14)	0.79(4)	S	$\tilde{F}66 = \tilde{F}48+\tilde{F}45$	18.70838(8)	121(14)	0.71(9)	S
$\tilde{F}23 = 2\tilde{F}13-\tilde{F}18$	27.30485(4)	271(14)	0.80(4)	S	$\tilde{F}67 = \tilde{F}46+\tilde{F}16$	31.65667(8)	121(14)	0.17(9)	S
$\tilde{F}24 = 2\tilde{F}16-\tilde{F}8$	11.94672(3)	270(14)	0.10(4)	P	$\tilde{F}68 = \tilde{F}34-\tilde{F}41$	27.27566(8)	117(14)	0.55(10)	S
$\tilde{F}25 = \tilde{F}15+2f_{orb}$	27.22180(4)	257(14)	0.95(4)	S	$\tilde{F}69 = \tilde{F}18-4f_{orb}$	18.75596(8)	115(14)	0.90(10)	S
$\tilde{F}26 = \tilde{F}2-f_{orb}$	11.02619(4)	257(14)	0.61(4)	S	$\tilde{F}70 = \tilde{F}62+\tilde{F}1$	33.55675(8)	113(14)	0.61(10)	P
$\tilde{F}27$	19.80505(4)	254(14)	0.52(4)	P	$\tilde{F}71 = 2\tilde{F}62-\tilde{F}14$	19.37004(9)	108(14)	0.09(10)	P
$\tilde{F}28$	30.10362(4)	250(15)	0.36(5)	P	$\tilde{F}72$	33.11220(9)	106(14)	0.24(10)	P
$\tilde{F}29 = \tilde{F}22-2f_{orb}$	24.43831(4)	241(14)	0.29(4)	S	$\tilde{F}73 = \tilde{F}17+\tilde{F}17$	2.41278(9)	103(14)	0.15(11)	P
$\tilde{F}30$	26.93403(4)	216(14)	0.28(5)	S	$\tilde{F}74 = 2\tilde{F}50+\tilde{F}2$	16.39267(9)	103(14)	0.12(11)	S
$\tilde{F}31$	25.79580(4)	209(14)	0.32(5)	S	$\tilde{F}75 = 2\tilde{F}25-2\tilde{F}1$	32.30819(9)	102(14)	0.88(11)	S
$\tilde{F}32 = \tilde{F}29-\tilde{F}24$	12.49488(5)	205(14)	0.81(6)	P	$\tilde{F}76 = 2\tilde{F}14-\tilde{F}18$	30.02491(9)	100(14)	0.07(11)	S
$\tilde{F}33 = \tilde{F}31-2f_{orb}$	24.59732(5)	202(14)	0.24(5)	S	$\tilde{F}77 = \tilde{F}68-\tilde{F}39$	1.16404(10)	100(15)	0.03(12)	S
$\tilde{F}34$	29.67910(5)	198(15)	0.31(6)	P	$\tilde{F}78 = \tilde{F}3-f_{orb}$	12.19408(10)	99(14)	0.97(12)	S
$\tilde{F}35 = \tilde{F}29-2\tilde{F}2$	1.18997(6)	196(15)	1.00(8)	S	$\tilde{F}79 = \tilde{F}77+\tilde{F}73$	3.58210(9)	98(14)	0.07(11)	S
$\tilde{F}36 = 2\tilde{F}8-\tilde{F}23$	23.96719(5)	192(14)	0.86(6)	S	$\tilde{F}80 = \tilde{F}24+2f_{orb}$	13.14177(10)	98(14)	0.29(11)	P
$\tilde{F}37 = \tilde{F}36-\tilde{F}24$	12.01960(5)	192(14)	0.16(7)	S	$\tilde{F}81 = \tilde{F}75-\tilde{F}46$	19.43518(10)	98(14)	0.45(11)	P
$\tilde{F}38 = 2\tilde{F}29-\tilde{F}16$	30.09070(5)	188(15)	0.85(7)	P	$\tilde{F}82 = \tilde{F}1+f_{orb}$	11.67065(10)	98(14)	0.12(11)	S
$\tilde{F}39 = \tilde{F}23-2f_{orb}$	26.10774(5)	187(14)	0.91(6)	S	$\tilde{F}83 = \tilde{F}81+2f_{orb}$	20.63132(10)	95(14)	0.41(12)	P
$\tilde{F}40 = \tilde{F}32-f_{orb}$	11.89424(5)	186(14)	0.90(6)	P	$\tilde{F}84 = 2\tilde{F}50+\tilde{F}10$	16.76843(10)	90(14)	0.37(12)	P
$\tilde{F}41 = 2\tilde{F}17$	2.40322(5)	180(14)	0.46(6)	S	$\tilde{F}85 = \tilde{F}77+\tilde{F}2$	12.78374(12)	86(14)	0.55(16)	S
$\tilde{F}42 = \tilde{F}36+4f_{orb}$	26.36587(5)	180(14)	0.78(6)	P	$\tilde{F}86 = \tilde{F}4-f_{orb}$	19.52187(23)	40(14)	0.85(27)	S
$\tilde{F}43 = 2\tilde{F}35+\tilde{F}41$	4.78393(5)	177(14)	0.59(6)	S	$\tilde{F}87 = \tilde{F}2-3f_{orb}$	9.8310(4)	26(14)	0.5(4)	S
$\tilde{F}44 = 2\tilde{F}24-\tilde{F}37$	11.87541(5)	173(14)	0.96(6)	S	$\tilde{F}88 = \tilde{F}2-f_{orb}$	12.2242(4)	21(15)	0.6(5)	S

Notes. The values in parentheses give the 1σ uncertainty as a combination of the values reported by the least square algorithm and the standard error estimates formulated by Montgomery & O'Donoghue (1999). f_{orb} is the orbital frequency. C is a shortcut for Component and denotes either the primary (P) or secondary (S) whichever was chosen according to the test statistics. From these 88 frequencies, 30 were assigned to the primary and 58 to the secondary component.

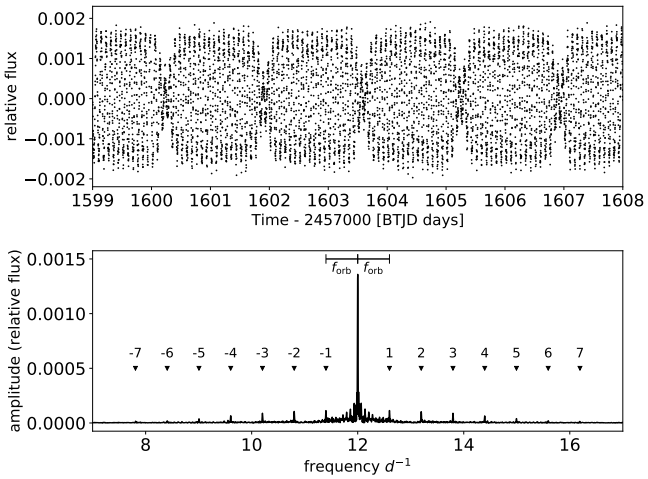

Fig. C.1. Top panel: simulated light curve for one frequency originating from the secondary component. Bottom panel: amplitude spectra of the light curve in the top panel. Side-frequencies are marked with a triangle and annotate with the number of orbital frequencies that they are shifted with. The errorbars on top show the extend of one orbital frequency.

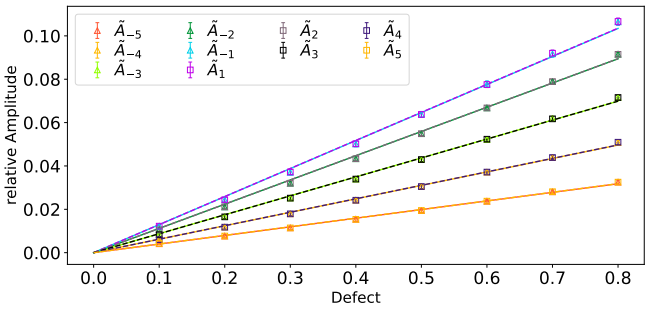

Fig. C.2. The relative amplitude of the side peaks as a function of the defect where different colors correspond to different side peaks as given by the legend. The uncertainties are typically the size of the markers. Lines correspond to linear fits that agree within 2 sigma with a reduced χ^2 statistics of 1 for all fits.

Appendix C: Superposition of modes with phase dependent Amplitude: A deeper Look

To show the effect of the phase dependent amplitude as in equation (2), we simulated a light curve for a frequency of 12 $d^{-1}$with an amplitude of 1500 ppm for the secondary star for an amplitude decrease of 0.7 and a standard deviation of the Gaussian of 0.05. The results are shown in Figure C.1. The amplitude of the signal is clearly modulated during the time of secondary eclipse. This results in a splitting of the signal in the amplitude spectra, where the peaks are distanced by $if_{\rm orb}$ with $i \in [-7, -6, -5, -4, -3, -2, -1, 1, 2, 3, 4, 5, 6, 7]$. All of this peaks are also extracted from a modelling process according the model equation (1).

We furthermore simulated 1000 light curves for different amplitude decrease between 0.1 and 0.8 in steps of 0.1 with different frequencies in the range $10 \leq f \leq 20$ and ampltiudes in the range $1000 \leq \tilde{A} \leq 3000$ ppm. We modeled all these light curve using equation (1) and analysis the results. For all the light curves, we found side peaks corresponding to $|i| \leq 5$. The corresponding amplitudes relative to the input amplitudes are shown in Figure C.2 and denoted with $\tilde{A}_i$. The relative amplitude is in a first approximation linearly dependent on the defect and symmetric, that is $\tilde{A}_i = \tilde{A}_{-i}$. Fitting the data points with a polynomial of degree2, the values become overfitted according to the reduced χ^2 statistics.